Kent Academic Repository

Dufloo, Jérémy, Fernández, Ignacio, Arbabian, Atousa, Haouz, Ahmed, Temperton, Nigel J., Gimenez-Lirola, Luis G., Rey, Félix A. and Sanjuán, Rafael (2025) ***Dipeptidase 1 is a functional receptor for a porcine coronavirus.*** **Nature Microbiology . ISSN 2058-5276.**

Downloaded from

https://kar.kent.ac.uk/111586/ The University of Kent's Academic Repository KAR

The version of record is available from

https://doi.org/10.1038/s41564-025-02111-7

This document version

Publisher pdf

DOI for this version

Licence for this version

CC BY-NC-ND (Attribution-NonCommercial-NoDerivatives)

Additional information

Versions of research works

Versions of Record

If this version is the version of record, it is the same as the published version available on the publisher's web site. Cite as the published version.

Author Accepted Manuscripts

If this document is identified as the Author Accepted Manuscript it is the version after peer review but before type setting, copy editing or publisher branding. Cite as Surname, Initial. (Year) 'Title of article'. To be published in ***Title of Journal*** , Volume and issue numbers [peer-reviewed accepted version]. Available at: DOI or URL (Accessed: date).

Enquiries

If you have questions about this document contact ResearchSupport@kent.ac.uk. Please include the URL of the record in KAR. If you believe that your, or a third party's rights have been compromised through this document please see our Take Down policy (available from https://www.kent.ac.uk/guides/kar-the-kent-academic-repository#policies).

nature microbiology

Article

https://doi.org/10.1038/s41564-025-02111-7

Dipeptidase 1 is a functional receptor for a porcine coronavirus

Received: 20 December 2024

Accepted: 11 August 2025

Jérémy Dufloo[1,6], **Ignacio Fernández**[2,6], **Atousa Arbabian**[2], **Ahmed Haouz**[3], **Nigel Temperton**[4], **Luis G. Gimenez-Lirola**[5], **Félix A. Rey**[2] ✉ & **Rafael Sanjuán**[1] ✉

Coronaviruses of the subgenus *Embecovirus* include several important pathogens, such as the human seasonal coronaviruses HKU1 and OC43, bovine coronavirus and porcine haemagglutinating encephalomyelitis virus (PHEV). While sialic acid is thought to be required for embecovirus entry, protein receptors remain unknown for most of these viruses. Here we show that PHEV does not require sialic acid for entry and instead uses dipeptidase 1 (DPEP1) as a receptor. Cryo-electron microscopy at 3.4–4.4 Å resolution revealed that, unlike other embecoviruses, PHEV displays both open and closed conformations of its spike trimer at steady state. The spike receptor-binding domain (RBD) exhibits extremely high sequence variability across embecoviruses, and we found that DPEP1 usage is specific to PHEV. In contrast, the X-ray structure of the RBD–DPEP1 complex at 2.25 Å showed that the structural elements involved in receptor binding are conserved, highlighting the remarkable versatility of this structural organization in adopting novel receptor specificities.

The betacoronavirus 1 species includes ten host-specific viruses infecting farm animals, such as the porcine haemagglutinating encephalomyelitis virus (PHEV) and bovine coronavirus (BCoV), but also other mammals including humans, where they cause seasonal colds (human coronavirus OC43) or diarrhoea (human enteric coronavirus strain 4408). The betacoronavirus 1 species belongs to the *Embecovirus* subgenus, which includes additional relevant viruses such as the human common cold virus HKU1 and murine hepatitis virus (MHV). It is believed that present-day embecoviruses derive from ancestral rodent viruses that diversified through cross-species transmission[1]. For example, it has been estimated that BCoV and OC43 diverged over a century ago following a zoonotic or reverse zoonotic event[2].

The entry of embecoviruses and other coronaviruses into host cells is mediated by the spike protein trimer, which binds to a specific receptor and triggers fusion of viral and cellular membranes. The C-terminal domain of the spike S1 subunit typically acts as a protein-receptor binding domain (RBD)[3], but receptors remain unknown for most embecoviruses, including all members of the betacoronavirus 1 species. For many coronaviruses, the RBD can adopt 'up' and 'down' conformations that determine spike opening, which is a pre-requisite for membrane fusion. However, all embecovirus spikes, including those of MHV[4], OC43 (ref. 5) and HKU1 (ref. 6), have been observed exclusively in closed conformation at steady state, suggesting that binding to a ligand is necessary to promote or stabilize spike opening and allow viral entry, as shown for HKU1 (ref. 7).

The N-terminal domain (NTD) of the embecovirus spike S1 subunit harbours a conserved glycan-binding site used for attachment to cells, which interacts with 9-*O*-acetyl-sialic acid as shown for HKU1, OC43, BCoV and PHEV[8,9], an interaction that is necessary for HKU1, OC43 and BCoV entry[5,8]. The importance of glycan attachment is further highlighted by the presence of a haemagglutinin esterase (HE) on the embecovirus envelope, which is analogous to the influenza C/D

---

[1]Institute for Integrative Systems Biology, CSIC-Universitat de València, Paterna, València, Spain. [2]Institut Pasteur, Université Paris Cité, CNRS UMR 3569, Structural Virology Unit, Paris, France. [3]Institut Pasteur, Université Paris Cité, CNRS UMR 3528, Crystallography Facility-C2RT, Paris, France. [4]Viral Pseudotype Unit, Medway School of Pharmacy, Universities of Kent and Greenwich, Chatham, UK. [5]Department of Veterinary Diagnostic and Production Animal Medicine, Iowa State University, Ames, IA, USA. [6]These authors contributed equally: Jérémy Dufloo, Ignacio Fernández. ✉e-mail: felix.rey@pasteur.fr; rafael.sanjuan@uv.es

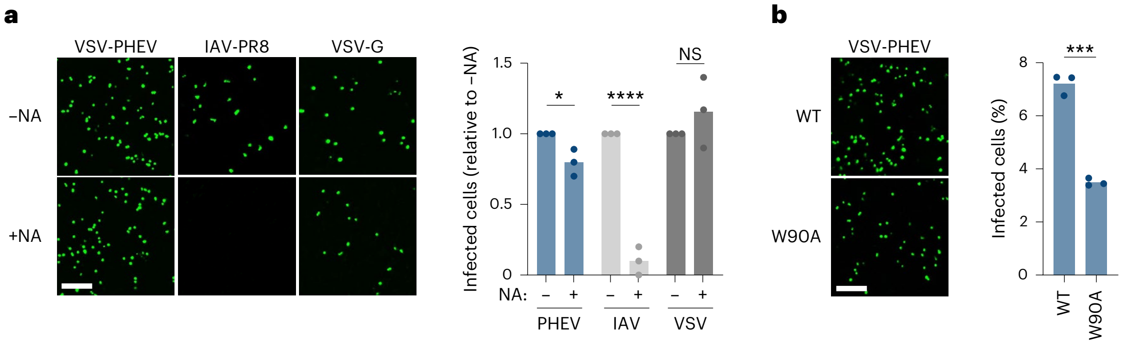

Fig. 1 | PHEV does not require sialic acid for entry. a, HCT-15 cells were treated or not with neuraminidase and infected with VSV-G and PHEV VSV pseudotypes or IAV (PR8-GFP). Left: representative images (scale bar, 200 µm). Right: ratio of infected cells relative to no-NA treatment. Each dot represents an independent experiment ($n = 3$). **b**, HCT-15 cells were infected with a WT or W90A PHEV spike mutant pseudotype. Left: representative images (scale bar, 200 µm). Right: percentage of infected cells. Each dot indicates a technical replicate ($n = 3$). The bars represent the mean, and the levels of statistical significance of two-sided unpaired *t*-tests are shown: ****$P < 0.0001$, ***$P < 0.001$, *$P < 0.05$; NS, not significant. In **a**, PHEV: $P = 0.021$; VSV: $P = 0.34$. In **b**, $P = 0.0001$.

haemagglutinin-esterase-fusion protein[10,11]. Although the presence of HE suggests that sialoglycans might function as embecovirus receptors, recent findings on HKU1 reveal a more complex scenario. HKU1 enters cells through a two-step process in which binding of the S1 NTD to 9-*O*-acetyl-sialic acids[8,12,13] triggers spike opening[7], allowing the RBD to bind to transmembrane protease serine 2 (TMPRSS2), which acts as a functional HKU1 receptor[14–17]. Nevertheless, whether the entry of other embecoviruses dually depends on binding to sialic acids and a cell surface protein remains unknown.

Here we identified dipeptidase 1 (DPEP1) as a functional receptor for coronavirus PHEV. We showed that, contrary to HKU1 and other betacoronavirus 1 members, the PHEV spike does not require binding to sialic acid for entry. We thoroughly characterized DPEP1 as a sufficient PHEV receptor and obtained the X-ray structure of the PHEV RBD in complex with DPEP1. Cryo-electron microscopy (cryo-EM) of the PHEV spike trimer revealed that, in contrast to other embecoviruses, it can be found in open conformations in the absence of ligand binding. We also found that RBD sequences vary extensively within the betacoronavirus 1 species and that DPEP1 usage is specific to PHEV. In contrast, the structural elements involved in receptor binding are conserved across embecoviruses. Our results highlight the diversity of embecovirus entry mechanisms and reveal that the RBD is capable of accommodating highly divergent sequences to enable receptor shifts.

Results

Sialic acid is dispensable for PHEV spike-mediated viral entry

Given the importance of sialic acid binding for embecovirus entry[8], we tested whether sialic acid was required for PHEV entry. To this aim, HCT-15 cells were pretreated with neuraminidase (NA) to remove all (α2,3)-, (α2,6)- and (α2,8)-linked sialic acids before infection with a vesicular stomatitis virus (VSV) pseudotype bearing the PHEV spike[18]. NA treatment only modestly decreased PHEV entry (20 ± 5.5% reduction compared with untreated cells; *t*-test: $P = 0.02$; Fig. 1a). Similarly, the W90A PHEV spike mutant, which cannot interact with sialic acid[8], showed only a 2-fold infectivity loss (7.22 ± 0.4% vs 3.5 ± 0.14% infected cells; *t*-test: $P = 0.0001$; Fig. 1b). In contrast, NA treatment reduced the entry of an HKU1 pseudotype by 40%, while a W89A HKU1 mutant, equivalent to the PHEV W90A mutation, completely lost infectivity (Extended Data Fig. 1). These results indicate that sialic acid may act as a PHEV attachment factor but is not strictly required for viral entry, in contrast to other betacoronavirus 1 members and HKU1.

Identification of a PHEV candidate receptor

The above results suggest that PHEV uses a protein receptor for entry. To identify potential candidates, we systematically quantified PHEV pseudotype infectivity in 48 human cell lines from the NCI-60 panel[18]. We observed infection in 16 out of 48 cell lines tested (Extended Data Fig. 2a,b and Supplementary Table 1). Since the NCI-60 panel has been previously characterized by transcriptomics[19,20], we correlated PHEV pseudotype infectivity with the expression levels of 7,694 genes encoding cell surface proteins (Extended Data Fig. 2c). The expression of 6 genes correlated positively and significantly with infectivity after adjusting for false discovery rates (Fig. 2a). The top hit was DPEP1 (Pearson $r = 0.766$, $P < 0.0001$; Fig. 2b), a GPI-anchored peptidase involved in renal metabolism[21].

DPEP1 sensitizes cells to PHEV spike-mediated viral entry

We next examined the effect of human DPEP1 (hDPEP1) transfection on PHEV pseudotype infectivity in HEK293T cells. Transfection increased infection rates from undetectable levels (0.07 ± 0.04%) to 54 ± 3.6% (*t*-test: $P < 0.0001$; Fig. 2c). This effect was specific to PHEV, as infection with empty, VSV-G, SARS-CoV-2 or MERS-CoV pseudotypes was unaffected (Fig. 2c and Extended Data Fig. 2d). We confirmed these results in seven additional cell lines, where we observed an average 73-fold increase in PHEV pseudotype infection upon hDPEP1 transfection (Fig. 2d). Conversely, CRISPR-Cas9-mediated knockout of DPEP1 in susceptible HCT-15 cells markedly inhibited the entry of PHEV pseudotypes (Fig. 2e). We also used a GFP complementation assay to assess whether expression of the spike at the cell surface triggered syncytia formation. This showed that co-expression of hDPEP1 and the PHEV spike allowed strong syncytia formation (Fig. 2f). Since PHEV is a porcine virus, we confirmed that pig DPEP1 (pDPEP1) supported PHEV pseudotype infection and spike-mediated cell–cell fusion to a similar or slightly lower extent than hDPEP1, respectively (Fig. 2g). Overall, these experiments demonstrate that the porcine and human versions of DPEP1 sensitize cells to PHEV spike-mediated viral entry and induce spike-mediated cell–cell fusion.

DPEP1 binds the PHEV spike

Since DPEP1 is a peptidase, we first sought to determine whether it acted as a PHEV receptor or promoted entry by priming the spike. To this end, we generated the catalytically inactive mutant E141D[22]. This mutant was capable of mediating viral entry into transfected HEK293T cells and induced PHEV spike-mediated cell–cell fusion similarly to wild-type (WT) hDPEP1, showing that the peptidase activity of DPEP1 is dispensable to promote PHEV entry (Fig. 3a). We then examined whether DPEP1 directly bound the PHEV spike. For this, we first incubated PHEV spike-transfected HEK293T cells with increasing concentrations of soluble recombinant hDPEP1 and measured hDPEP1 binding by flow cytometry (Fig. 3b). We observed a strong dose-dependent binding of soluble hDPEP1 to spike-expressing cells. We then expressed the PHEV spike RBD (residues 327–605) to measure

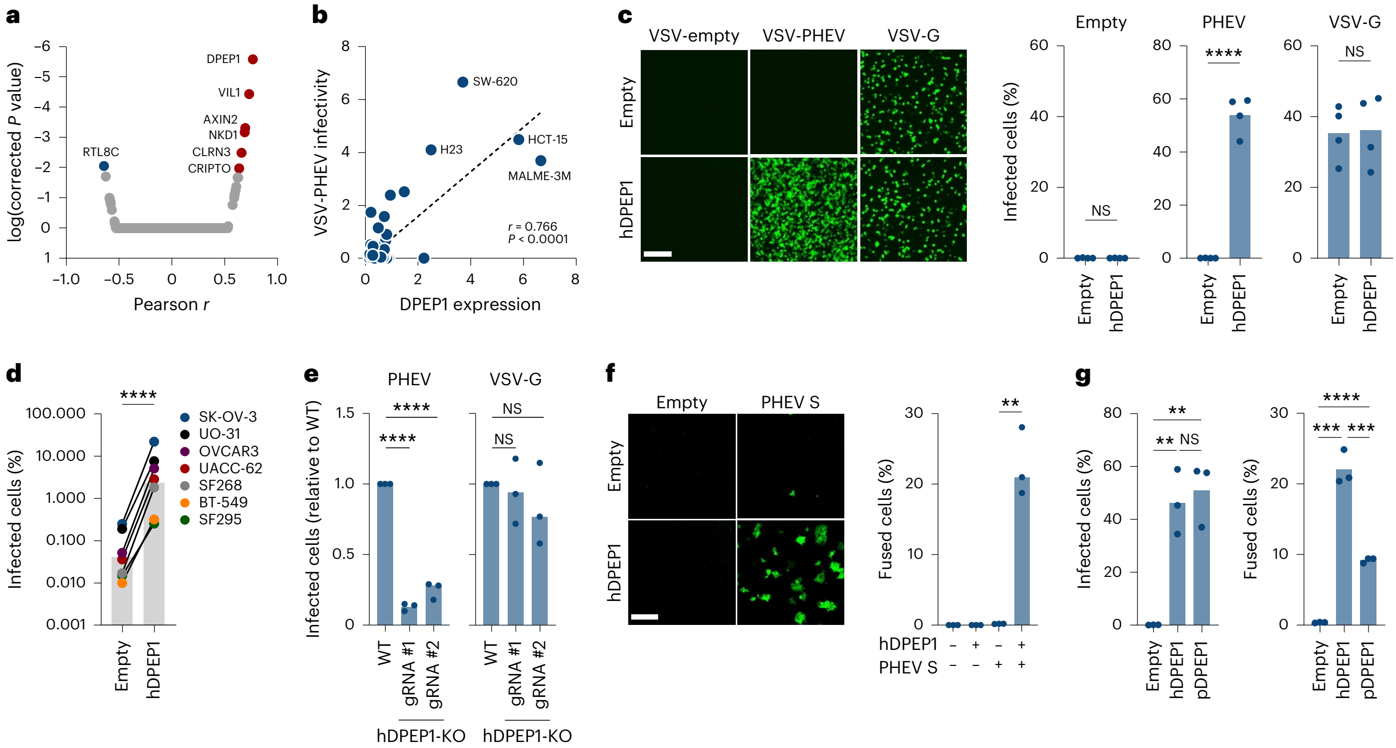

Fig. 2 | DPEP1 triggers PHEV spike-mediated fusion. a, PHEV pseudotype infectivity in the NCI-60 panel was correlated with the expression of 7,694 genes encoding membrane-associated proteins. The Pearson correlation coefficients and the Bonferroni-corrected *P* values for each gene are shown. Each dot represents a different gene ($n = 7{,}694$). Genes in red and blue are the ones with significant ($P < 0.01$; two-sided) positive and negative correlation with infectivity, respectively. The names of these genes are indicated. **b**, Correlation between the expression of DPEP1 and PHEV infectivity in the NCI-60 cell lines. Each point corresponds to a different cell line ($n = 47$). The names of the cell lines with the highest DPEP1 expression level and VSV-PHEV infectivity are indicated. Pearson *r* and two-sided *P* value are indicated. **c**, HEK293T cells were transfected with hDPEP1-expressing plasmid or an empty vector and infected with empty, VSV-G and PHEV VSV pseudotypes. Cells were imaged at 20 h post infection. Left: representative images (scale bar, 200 µm). Right: percentage of infected cells. Each dot represents an independent experiment ($n = 4$). **d**, Different cell lines were transfected with a human DPEP1 (hDPEP1)-expressing plasmid or an empty vector and infected with PHEV pseudotypes. The percentage of infected cells at 20 h post infection is shown. Each dot represents a different cell line ($n = 7$). The bar represents the mean, and the level of significance of a two-sided paired *t*-test is shown: $^{****}P < 0.0001$. **e**, DPEP1 was knocked out in human HCT-15 cells using CRISPR-Cas9 with two DPEP1-specific guide RNAs (gRNA #1 and gRNA #2). WT and hDPEP1-knockout (hDPEP1-KO) cells were infected with either PHEV (left) or VSV-G (right) pseudotypes. The data show the relative infection levels in DPEP1-KO cells compared to WT cells. Each dot represents an independent experiment ($n = 3$). **f**, Left: representative images of cell–cell fusion upon hDPEP1 and/or PHEV spike transfection (scale bar, 200 µm). Right: percentage of cell–cell fusion in cells overexpressing the PHEV spike and hDPEP1 or an empty control. Each dot represents a technical replicate ($n = 3$). **g**, Left: HEK293T cells were transfected with hDPEP1, pig DPEP1 (pDPEP1) or an empty vector, and infected with a PHEV pseudotype. The percentage of infected cells is shown. Each dot represents an independent experiment ($n = 3$). Right: HEK293T GFP-split cells were transfected with the PHEV spike and hDPEP1, pDPEP1 or an empty vector. The percentage of cell–cell fusion is shown. Each dot represents a technical replicate ($n = 3$). In **c** and **e**–**g**, the bar represents the mean, and the levels of statistical significance of two-sided unpaired *t*-tests are shown: $^{****}P < 0.0001$, $^{***}P < 0.001$, $^{**}P < 0.01$. In **c** for VSV-G, $^{NS}P = 0.913$. In **e**, for VSV-G gRNA #1: $^{NS}P = 0.692$; for VSV-G gRNA #2: $^{NS}P = 0.376$. In **f**, $P = 0.0013$. In **g** (left panel), hDPEP1 vs Empty: $P = 0.0013$; pDPEP1 vs Empty: $P = 0.0019$; pDPEP1 vs hDPEP1: $^{NS}P = 0.658$. In **g** (right panel), hDPEP1 vs Empty: $P = 0.0001$; pDPEP1 vs hDPEP1: $P = 0.0009$.

its affinity for the pDPEP1 ectodomain by biolayer interferometry (BLI; Fig. 3c). The immobilized PHEV RBD interacted with pDPEP1 but not with human ACE2 (hACE2), confirming the specificity of the interaction. To measure the binding affinity avoiding avidity effects, we immobilized pDPEP1 and used the monomeric soluble RBD at a range of concentrations, which allowed us to estimate an equilibrium dissociation constant (K_d) of 1.50 ± 0.31 µM (Fig. 3d,e). Binding to hDPEP1 showed similar affinity ($K_d = 2.99 \pm 0.83$ µM; Fig. 3f). We also expressed a recombinant PHEV spike ectodomain (residues 15–1,274) to confirm its interaction with pDPEP1 by BLI (Fig. 3g). Given that DPEP1 is a dimer and the spike protein is a trimer, we did not derive kinetic and affinity parameters, but the curves clearly demonstrate their interaction. Finally, we performed a competition assay in which PHEV pseudotypes were incubated with increasing amounts of soluble hDPEP1 before infection of susceptible cells (HCT-15 or hDPEP1-transfected HEK293T cells; Fig. 3h). Soluble hDPEP1 strongly inhibited PHEV pseudotype infection in both cell lines (IC_{50}: 0.03 µg ml^{-1} in HCT-15 and 0.04 µg ml^{-1} in HEK293T-hDPEP1 cells). These assays collectively show that the human and porcine orthologues of DPEP1 specifically interact with the PHEV spike.

Soluble DPEP1 interferes with authentic PHEV infection

Although PHEV propagation in cell culture is challenging, we set out to investigate the role of DPEP1 using the authentic virus instead of pseudotypes. We thus ran the competition assay described above with PHEV strain 67N (Extended Data Fig. 3a). We incubated the virus with soluble hDPEP1 before inoculation of PK-15 or swine primary kidney cells (SPKC) and followed the release of viral particles into the supernatant over time by quantitative PCR with reverse transcription (RT–qPCR). In PK-15 cells, there was significantly less virus in the supernatant at 24 and 48 h post inoculation when the virus was pre-incubated with soluble hDPEP1 (24 h: 2.3-fold, *t*-test: $P = 0.0053$; 48 h: 2.9-fold, $P = 0.0031$; Extended Data Fig. 3b). In SPKC cells, hDPEP1 pretreatment significantly reduced virus release at all timepoints by a factor ranging from 2.5- to

https://doi.org/10.1038/s41564-025-02111-7

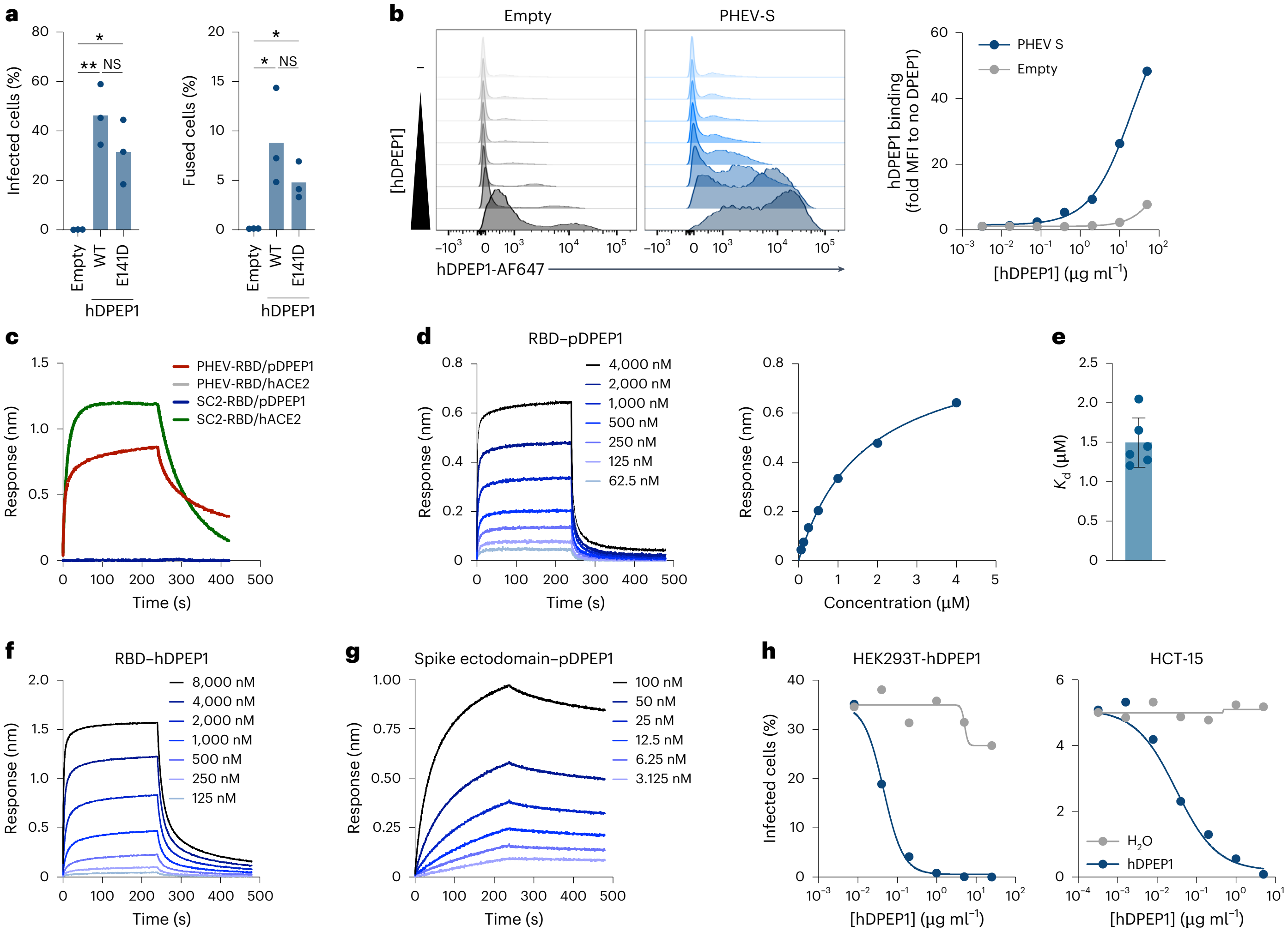

Fig. 3 | DPEP1 binds the PHEV spike. a, Left: HEK293T cells were transfected with WT or E141D hDPEP1 or an empty vector and infected with a PHEV pseudotype. The percentage of infected cells is shown. Each dot represents an independent experiment ($n = 3$). Right: HEK293T GFP-split cells were transfected with the PHEV spike and WT or E141D hDPEP1 or an empty vector. The percentage of cell–cell fusion is shown. Each dot represents a technical replicate ($n = 3$). Statistical significance determined using a two-sided unpaired *t*-test is shown: $^{*}P < 0.05$, $^{**}P < 0.01$. Left panel, WT vs Empty: $P = 0.0028$; E141D vs Empty: $P = 0.014$; WT vs E141D: $^{\mathrm{NS}}P = 0.227$. Right panel, WT vs Empty: $P = 0.038$; E141D vs Empty: $P = 0.0134$; WT vs E141D: $^{\mathrm{NS}}P = 0.258$. **b**, Flow cytometry measurement of soluble hDPEP1 binding to HEK293T cells transfected with the PHEV spike or an empty vector. Left: flow cytometry histogram of hDPEP1 binding in cells transfected with the PHEV spike or an empty vector. From top to bottom, cells were incubated without (−) and with increasing amounts of soluble hDPEP1. Right: the data shows the binding median fluorescence intensity (MFI) measured at each concentration of soluble hDPEP1 normalized to the MFI in the absence of hDPEP1, in cells transfected with an empty vector or the PHEV spike. Results from a representative experiment are shown. The gating strategy is shown in Supplementary Fig. 1. **c**, Binding of pDPEP1 or human ACE2 (hACE2) to PHEV or SARS-CoV-2 (SC2) RBD-coated sensors was quantified by BLI. One of two representative experiments is shown. **d**, Left: binding of pDPEP1 to PHEV RBD measured by BLI. pDPEP1 was immobilized on streptavidin sensors that were incubated with different RBD concentrations. Right: determination of the affinity of PHEV RBD for pDPEP1 using the steady-state method. The circles are experimental values and the line is the fitting of the experimental data. One of six representative experiments is shown. **e**, Affinity constants (K_d) of the PHEV RBD–pDPEP1 interaction obtained in the six independent experiments. Data are mean ± s.d. of K_d. **f**, Binding of hDPEP1 to PHEV RBD measured by BLI. hDPEP1 was immobilized on streptavidin sensors that were incubated with different RBD concentrations. **g**, Binding of immobilized pDPEP1 to the PHEV spike ectodomain measured by BLI using different spike concentrations. One of two representative experiments is shown. **h**, PHEV pseudotypes were incubated with the indicated concentration of soluble hDPEP1 (blue curve) or vehicle (grey curve, H_2O) before infecting HCT-15 (right) or hDPEP1-transfected HEK293T cells (left). Data show the percentage of infected cells at each soluble hDPEP1 concentration (mean of two technical replicates).

3.5-fold (*t*-tests: $P < 0.05$). These results therefore confirm the role of DPEP1 in PHEV infection.

TMPRSS2 enhances DPEP1-mediated entry but is not a receptor for PHEV

The only other protein described to bind an embecovirus RBD is TMPRSS2, which serves as a functional receptor for HKU1 (ref. 14). Moreover, TMPRSS2 activates the spike and enhances the entry of other coronaviruses such as SARS-CoV-2 (ref. 23) and MERS-CoV[24]. Therefore, we investigated its role in PHEV entry. We found that the expression of TMPRSS2 also correlated with PHEV pseudotype infectivity across the 48 cell lines of the NCI-60 panel, albeit less strongly than DPEP1 (Pearson $r = 0.47$, $P = 0.0009$; Extended Data Figs. 2c and 4a). Overexpression of human TMPRSS2 (hTMPRSS2) alone was not sufficient to promote PHEV pseudotype infection in three non-susceptible cell lines (HEK293T, SK-OV-3 and SF-268; Extended Data Fig. 4b). However, co-expression of hDPEP1 and hTMPRSS2 increased viral entry in all three cell lines compared with hDPEP1 alone (3.6-, 1.6- and 1.9-fold increase, respectively; Extended Data Fig. 4b). Co-expression of hDPEP1 and hTMPRSS2 also resulted in a 60% increase in spike-mediated cell–cell fusion compared with hDPEP1 alone (Extended Data Fig. 4c). These results show that TMPRSS2 enhances DPEP1-dependent entry but is unlikely to be a functional receptor for PHEV, indicating that receptor usage is not conserved between the HKU1 and PHEV embecoviruses. Finally, we used camostat mesylate (a serine protease inhibitor) and E-64d (a cysteine protease inhibitor) to further test the role of proteases in PHEV entry. Camostat treatment did not inhibit entry in HCT-15 cells, whereas E-64d reduced entry by more than 60%, suggesting that PHEV primarily uses cysteine proteases for entry (Extended Data Fig. 4d). These results suggest that although TMPRSS2 overexpression enhances viral entry, other proteases probably play a more decisive role in PHEV entry.

DPEP1 is a PHEV-specific receptor

Given that no betacoronavirus 1 receptor has been identified so far, we set out to determine whether DPEP1 was a general receptor for the species. To test this, we first measured the binding of recombinant hDPEP1 to cells overexpressing the OC43, BCoV, canine respiratory coronavirus (CRCoV) or equine coronavirus (ECoV) spike. The HKU24 spike was included as a non-betacoronavirus 1 embecovirus. Despite the detectable expression of all spikes, hDPEP1 binding could only be measured in PHEV-transfected cells, suggesting that DPEP1 is a PHEV-specific receptor (Extended Data Fig. 5a). To determine whether interspecies sequence variations in DPEP1 affect the ability of other betacoronavirus 1 members to use it as a receptor, we performed a cell–cell fusion assay using the spikes from PHEV, OC43, BCoV and CRCoV and the DPEP1 orthologues from their respective host species (*Homo sapiens*, *Sus scrofa*, *Canis lupus* and *Bos taurus*; Extended Data Fig. 5b). All four DPEP1 orthologues mediated cell–cell fusion only in the presence of the PHEV spike and not with the other three spikes, further supporting a PHEV-specific DPEP1 usage. To understand whether potential spike diversity might explain this receptor usage specificity, we built a phylogenetic tree of all embecovirus spike proteins (Extended Data Fig. 6a). Although betacoronavirus 1 spikes form a monophyletic group, PHEV and ECoV differed from the rest of betacoronavirus 1 members. In particular, a region of ~35 residues in their RBD was highly divergent from all other betacoronavirus 1 spikes and from each other (residues 499–534 of the PHEV spike; Extended Data Fig. 6b). Indeed, this region exhibited no significant similarity with any other viral sequence deposited in GenBank, and the structure-based remote homology detection tool pLM-Blast[25] showed no obvious hits.

X-ray structure of the PHEV RBD in complex with DPEP1

We attempted to predict the structure of the pDPEP1/PHEV RBD complex using AlphaFold3 (ref. 26), but the resulting interface confidence metrics for the predicted complex were very low (ipTM score: <0.3). We therefore crystallized the PHEV RBD in complex with pDPEP1 and determined the X-ray structure at 2.25-Å resolution (Supplementary Table 2). The asymmetric unit of the crystal contained one pDPEP1 dimer with two RBDs bound (Fig. 4a). pDPEP1 has an α/β barrel architecture that conserves the secondary structure elements, overall fold (root mean square deviation, RMSD: 0.931 Å for 5,446 atoms) and glycosylation sites (N57 and N279) of the human orthologue crystallized previously (PDB: 1ITQ)[27]. The active site has two zinc ions, one coordinated by H36, D38 and E141 and the second by H214, H235 and E141. The site of interaction with the RBD is on the face opposite to the active site and is formed by helices α_a, α_{2a} and α_e (Fig. 4b and Extended Data Fig. 7). The PHEV receptor binding site is in the RBD distal region, which has the shape of an open mouth (Fig. 4b). The upper jaw (jaw 1, j1) is formed by a long loop (residues 506–518), and the lower jaw (jaw 2, j2) consists of the η1 helical turn (residues 531–533, Extended Data Fig. 8) in the highly variable region observed in betacoronavirus 1 RBDs (Extended Data Fig. 6b). The interface between the PHEV RBD and pDPEP1 buries ~1,150 Å^2 (530 Å^2 on the RBD and 620 Å^2 on the receptor), an area considerably smaller than the buried surface area of other betacoronavirus RBD/receptor complexes[15]. The surface electrostatic potential shows moderate charge complementarity between the PHEV RBD and pDPEP1, with most of the RBD interface having no net charge, except for a few positive patches that face negative surfaces on pDPEP1 (Fig. 4c). The complex is stabilized by polar interactions that include five hydrogen bonds, with R130$_{\mathrm{pDPEP1}}$ and E351$_{\mathrm{pDPEP1}}$ participating in most of them, and a salt bridge (Supplementary Table 3 and Fig. 4d). Besides, two aromatic residues from the RBD (F507$_{\mathrm{RBD}}$ and W533$_{\mathrm{RBD}}$) stack against the long aliphatic side chains of arginine residues from pDPEP1 (Fig. 4d). Altogether, the small buried surface area of the interface, the limited charge complementarity and the scarcity of polar interactions are consistent with the measured binding affinity in the low micromolar range.

Structural conservation between the RBDs of PHEV and HKU1

Structural alignment of the PHEV RBD with those from OC43 (ref. 28) (PDB: 8TZU), MHV[29] (PDB: 6VSJ) and HKU1 (ref. 30) (PDB: 5KWB) revealed a shared fold, as indicated by low Cα root mean square deviation (CA-RMSD) values and high pairwise alignment *Z*-scores obtained from the Dali server[31] (Fig. 4e). This common fold consists of two subdomains: a core (PHEV residues 327–434 and 583–603) that has a topology similar to the RBDs from other betacoronaviruses (SARS-CoV, MERS-CoV) and an insertion (PHEV residues 435–582) that is unique to embecoviruses and encompasses the highly divergent region presented above (Extended Data Fig. 6b). Several segments of the insertion subdomains from different RBDs superpose well (Fig. 4e), except for the highly variable region located toward the RBD tip, where the DPEP1 contact residues are located. The RBD tip also harbours the TMPRSS2 binding site in the HKU1 RBD[15] (Fig. 4e), and the same structural elements adopt slightly different conformations to participate in the interaction (Fig. 4f). The RBD sequences from betacoronavirus 1 members have deletions in the positions corresponding to the receptor-binding site (Extended Data Fig. 8), which could be responsible for their different receptor specificities. The most extensive deletion is found in the OC43 variable region, corresponding to the PHEV j1 segment (Fig. 4e and Extended Data Fig. 8).

Functional identification of critical residues for DPEP1–PHEV spike interaction

To test the role of specific residues at the PHEV spike–DPEP1 interface in virus entry, we performed site-directed mutagenesis of the PHEV spike and pDPEP1 and evaluated the ability of these mutants to mediate pseudotype entry and cell–cell fusion (Fig. 5a,b). First, we mutated ten interface residues of the PHEV spike and included variant Q487A (mapping to the loop below j1 and not in contact with DPEP1) for comparison. Strikingly, the F507R and W533A spike mutants almost completely abolished PHEV pseudotype infectivity in pDPEP1-expressing cells and led to a >10-fold reduction in cell–cell fusogenicity (Fig. 5a). Other mutations (V510R, T511D, T514A and T517R) decreased pseudotype infectivity to a lower extent (5- to 38-fold) without decreasing cell–cell fusion. Spike sequence diversity is low across PHEV strains (98.2% average conservation), particularly at DPEP1-interacting residues (Extended Data Fig. 9), suggesting that DPEP1 is probably used as a receptor by all PHEV variants. We then performed similar analyses by mutating three interface residues of pDPEP1 (T123, R126 and E351) and used mutant Q42A, a residue away from the RBD recognition site, for comparison. The E351R mutation completely abolished entry of a PHEV pseudotype and strongly reduced cell–cell fusion (Fig. 5b). Mutating this residue to alanine (E351A) also slightly decreased PHEV pseudotype entry but did not alter cell–cell fusogenicity. This residue is therefore critical for the PHEV spike–pDPEP1 interaction.

Cross-species variability in critical DPEP1 residues may explain PHEV susceptibility

We then investigated whether interspecies variation in contact residues (Extended Data Fig. 7) could alter the ability of diverse mammalian DPEP1 orthologues to promote PHEV entry. We first examined the

https://doi.org/10.1038/s41564-025-02111-7

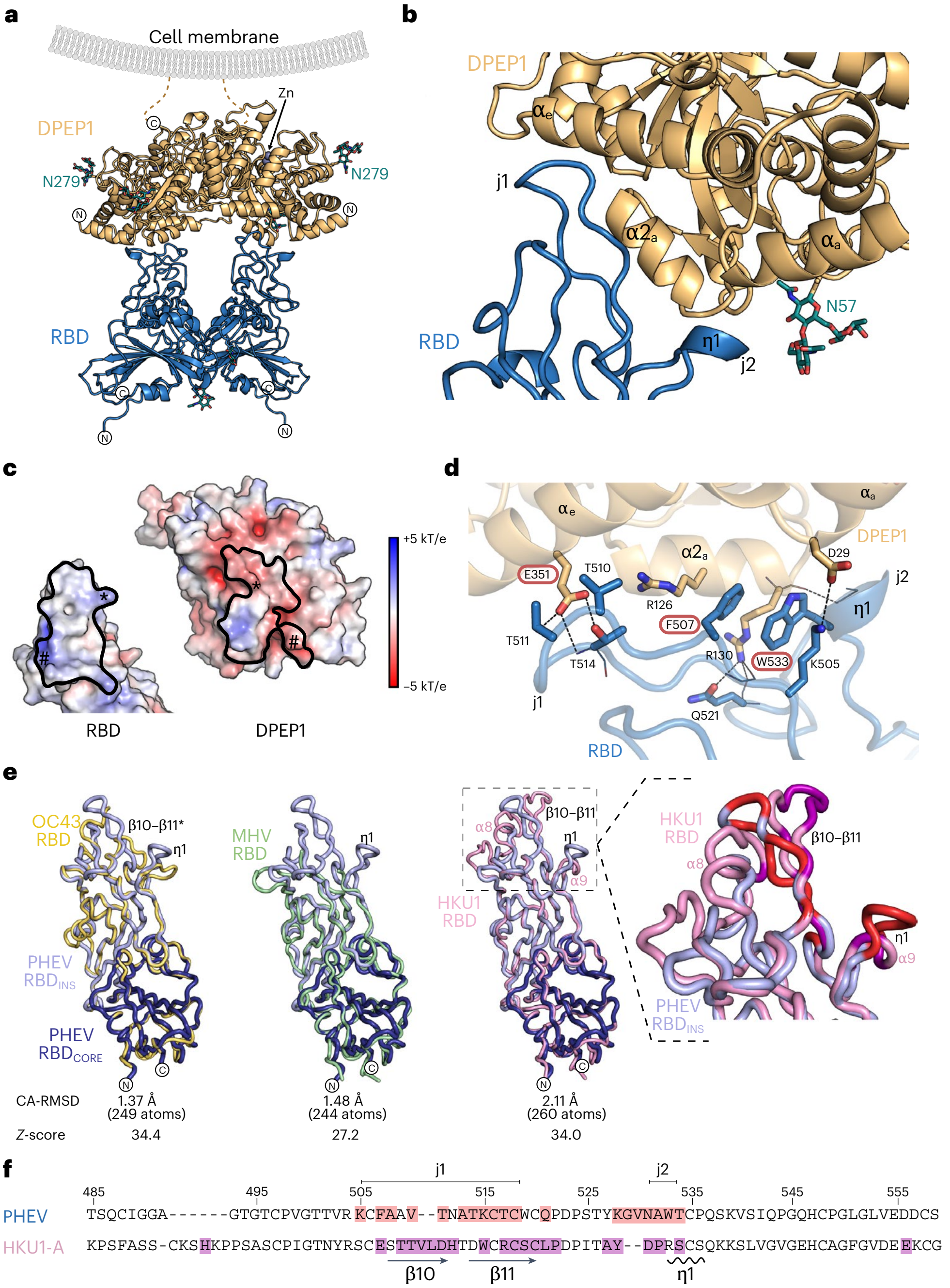

Fig. 4 | Crystal structure of the PHEV RBD in complex with porcine DPEP1. **a**, Structure of the isolated RBD–pDPEP1 complex. The N and C termini of the proteins are indicated with circled ‘N’ and ‘C’ letters, respectively. Glycans are represented with green sticks and the asparagine residues to which they are linked are indicated. The DPEP1 active site contains two zinc ions (grey spheres), and the orientation of the protein with respect to the plasma membrane is shown. The location of the cell membrane on which DPEP1 is inserted is indicated, showing that the RBD recognizes the opposite face. **b**, Close-up view of the RBD–pDPEP1 interface. The RBD tip adopts an open mouth shape with two jaws, j1 and j2. Secondary structure elements involved in the interaction are highlighted. The glycan attached to N57 is represented with green sticks. **c**, Open book representation of the PHEV RBD and pDPEP1 showing the surface electrostatic potential. The thick black line delimits the residues involved in the interface. The star (*) and hash (#) signs indicate the regions with complementary charge that are in contact. **d**, Detailed atomic interactions at the RBD– pDPEP1 interface. The side chains of relevant residues are shown in sticks, while main chain atoms are in thin lines. Dotted lines are used to represent hydrogen bonds or salt bridges. Some secondary structure elements are labelled, as well as j1 and j2. Relevant interface residues are indicated with red-outlined labels. **e**, Superposition of the PHEV RBD structure with those from OC43 (left, yellow, lPDB: 8TZU), MHV (middle, green, PDB: 6VSJ) and HKU1 (right, pink, PDB: 5KWB). The RBD subdomains are shown in the PHEV structure, with the core in dark blue (PHEV RBD$_{CORE}$) and the insertion in light blue (PHEV RBD$_{INS}$). Relevant secondary structure elements are labelled. An asterisk (*) is used to indicate correspondence with HKU1, even though the secondary structure is different. Below each alignment are the values of the root mean square deviation between alpha-carbons (CA-RMSD) and the *Z*-score of the pairwise alignment performed with the Dali server ($Z > 20$ indicates that the proteins are structural homologues[67]). The inset on the far-right zooms into the RBD tips (dashed box) from PHEV (light blue) and HKU1 (pink), where the RBD residues buried at the interface formed with pDPEP1 and TMPRSS2 are indicated in red and magenta, respectively, and relevant secondary structure elements are labelled. **f**, Amino acid sequence alignment of the PHEV and HKU1 RBDs, showing the residues buried by the receptor (shaded in red and violet, respectively). The numbers above the sequence indicate the residue numbering in the PHEV spike. Two arrows and a wavy line below the alignment indicate beta strands and an alpha helix, respectively, in the HKU1 RBD. This figure was created with BioRender (https://BioRender.com/rfqcbvd).

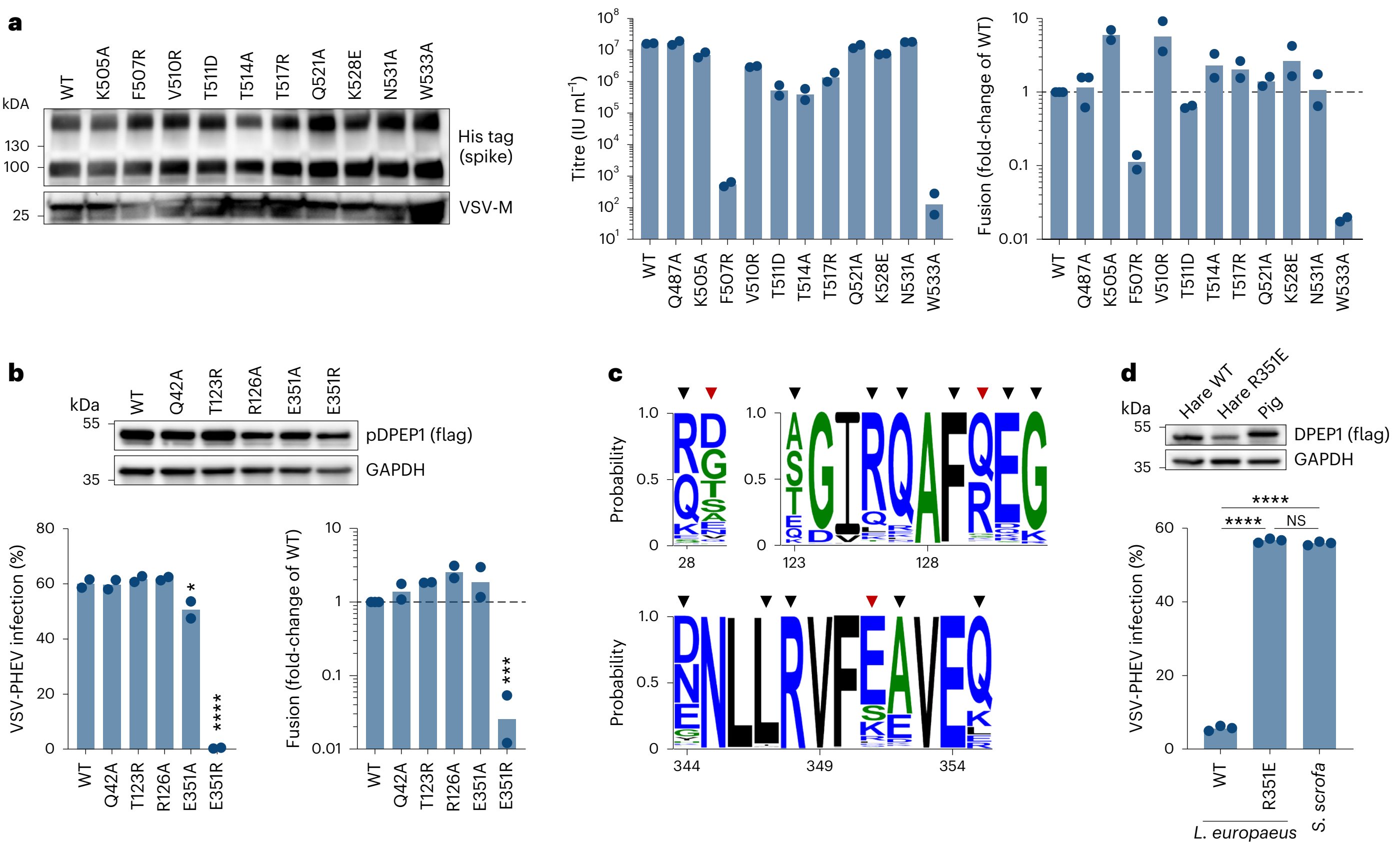

Fig. 5 | Identification of critical residues for the interaction between pDPEP1 and the PHEV spike. a, Left: western blot confirmation of the incorporation of the WT and mutant PHEV spikes into VSV pseudotypes. A His-tag added to the spike C terminus was used for detection and the VSV M protein was used as a loading control. Middle: PHEV pseudotypes were produced with WT or the indicated mutant spikes and titrated on HEK293T cells expressing pDPEP1. Pseudotype titres are shown. Right: HEK293T GFP-split cells were transfected with pDPEP1 and WT or mutant PHEV spikes. The fold change in cell–cell fusion relative to the WT is shown. **b**, Top: western blot confirmation of WT and mutant pDPEP1 expression. A Flag-tag added to the pDPEP1 C terminus was used for detection and GAPDH was used as a loading control. Bottom left: HEK293T were transfected with WT or mutant pDPEP1 and infected with PHEV pseudotypes. Percentages of infection are shown. Bottom right: HEK293T GFP-split cells were transfected with the PHEV spike and WT or mutant pDPEP1. The fold change in cell–cell fusion relative to the WT is shown. The statistical significance results of a one-way analysis of variance (ANOVA) with Dunnett's multiple comparisons test on log-transformed data are shown: *$P < 0.05$, ***$P < 0.001$, ****$P < 0.0001$. **c**, Probability of different amino acids occupying the indicated positions (numbers at the bottom) of mammalian DPEP1 orthologues ($n = 225$ mammal species). Inverted triangles indicate the residues involved in the interaction with the PHEV spike, with those in red forming polar interactions. **d**, HEK293T cells were transfected with the pig (*S. scrofa*, E351) or hare (*L. europaeus*) DPEP1, either WT (R351) or mutant (R351E), and infected with PHEV pseudotypes. The percentage of infected cells is shown. The statistical significance results of two-sided unpaired *t*-tests are indicated: ****$P < 0.0001$; $^{NS}P = 0.186$. The bar represents the mean and each dot is a technical replicate ($n = 3$). In **a** and **b**, the bar represents the mean, each dot represents an independent experiment ($n = 2$).

degree of conservation of DPEP1 interface residues in 225 mammalian species (Fig. 5c). Some contact residues were strongly conserved (for example, F129, L347, R348), but the majority, including the three residues involved in polar contacts with the PHEV RBD (D29, R130, E351), showed some degree of variability (Extended Data Fig. 7). In particular, some species such as the European hare (*Lepus europaeus*) have an arginine at position 351 (R351). In agreement with our mutagenesis results, the hare DPEP1 (haDPEP1) orthologue was poorly able to mediate entry of PHEV pseudotype into HEK293T cells (Fig. 5d). Mutating the arginine to a glutamic acid (R351E) conferred haDPEP1 the ability to mediate PHEV entry to the same level as pDPEP1 (Fig. 5d). These results confirm the functional importance of this residue for the interaction with the PHEV spike and suggest that it could be a determinant of PHEV cross-species transmissibility.

PHEV spike opening does not require sialoglycan binding

The spike protein from embecoviruses MHV, HKU1 and OC43 adopts a closed conformation in the absence of a sialic acid ligand[4–6]. Binding of the HKU1 spike NTD to specific sialoglycan ligands triggers an allosteric conformational change that promotes RBD opening[7,32] and exposure of the protein-receptor binding site[15]. To explore whether this is the case for PHEV, we studied its spike ectodomain by cryo-EM. The construct was stabilized by mutation of the furin site to impair cleavage, and by fusing a 'Foldon' trimerization motif[33] at the C terminus, but without the S2 stabilizing proline mutations used in other studies[34,35]. We found that in the apo state, the PHEV spike displays the RBD in different configurations, with roughly 25% of the trimers in the closed form (three RBDs in the down position), 50% in the 1-RBD-up state, 13% with 2-RBDs-up and 12% in the open form (3-RBDs-up; Fig. 6a, and Supplementary Fig. 2 and Table 4). Upon non-uniform refinement of the closed form, we obtained a cryo-EM map at an overall resolution of 3.4 Å (Supplementary Table 4). For the open conformations, as the number of up-RBDs increases, their density becomes weaker (identified in Fig. 6a as 'up/missing'), indicating that they are highly flexible in this conformation. Even in the closed form, we found that the cryo-EM densities for the RBD tip and the NTD upper subdomain containing the glycan-binding site were weak (Supplementary Fig. 2), and hence performed a focused refinement to improve their local resolution from ~6 Å to 4.4 Å, allowing model building (Fig. 6b and Supplementary Table 4). The model showed that, in the PHEV apo structure, the e1 loop delimiting the glycan-binding site

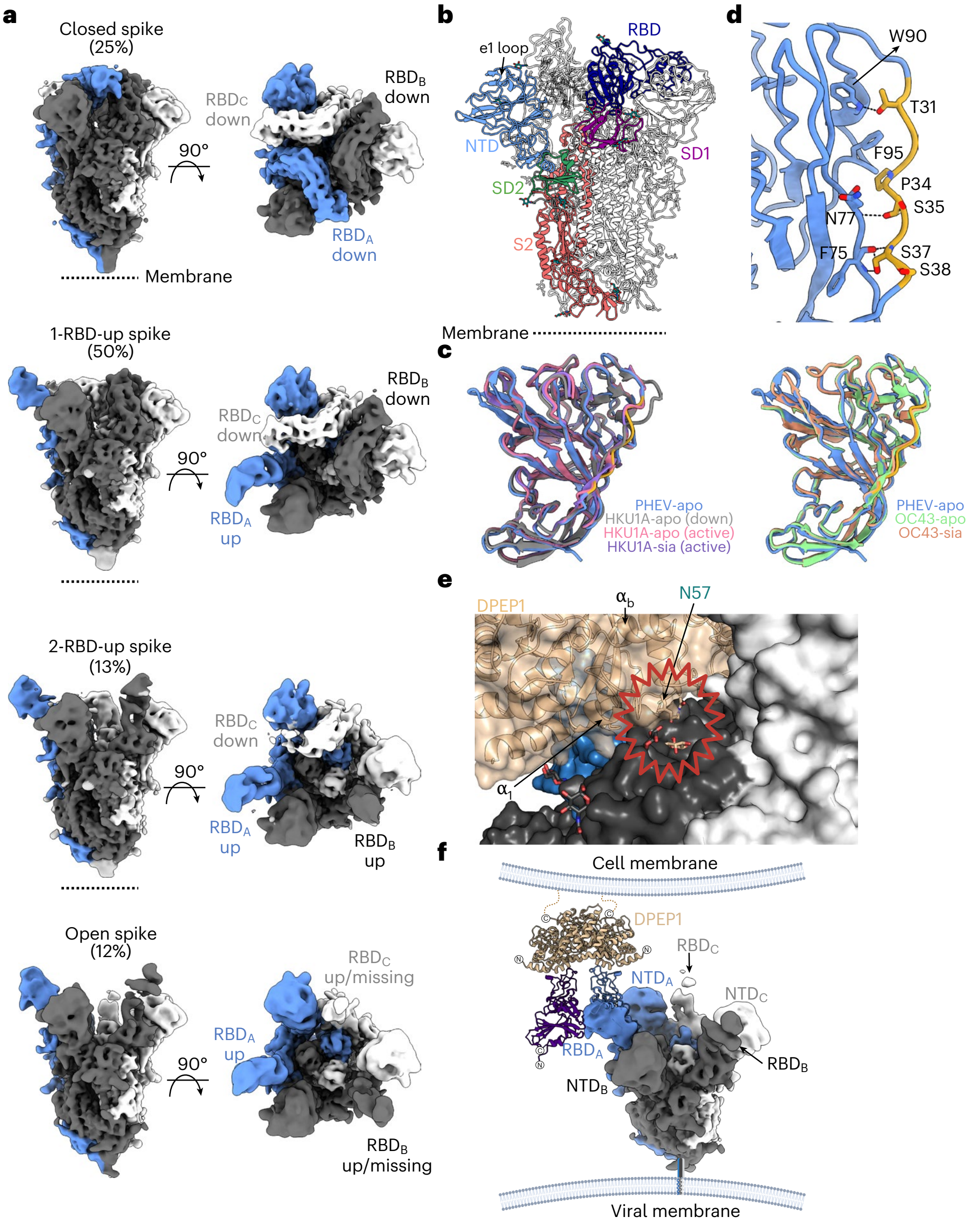

Fig. 6 | Cryo-EM of the PHEV spike ectodomain. a, Refined cryo-EM maps of different spike conformations obtained after 3D classification (Supplementary Fig. 2). The maps were filtered according to the local resolution to facilitate comparison. Left: side views of the spike where each protomer is shown in a different colour (blue, white and dark grey). A dashed line in each panel indicates the position of the viral membrane. Right: top view of the spike trimers, with a subscript (A, B, C) labelling the protomers. Each conformation is identified with the number of RBDs in the 'up' position, and the number in parentheses indicates the percentage of particles in each state. **b**, Cartoon representation of the atomic model of the PHEV spike ectodomain in the closed state. For clarity, two protomers are outlined and the third one shows S1 domains and the S2 subunit in different colours. **c**, Left: superposition of the PHEV NTD structure determined by local refinement of the closed spike in the absence of a glycan ligand (apo, blue) with HKU1A NTDs from a protomer in the down conformation not bound to a sialoglycan (apo-down, grey, PDB: 9BT2), from a protomer in a down yet active conformation without a bound glycan (apo-active, pink, PDB: 9BT9) and from a protomer in a down yet active conformation bound to a sialoglycan (Sia-active, violet, PDB: 9BTB). Right: structural superposition of the PHEV NTD from a closed spike protomer without a ligand (apo, blue), and OC43 NTDs from closed spikes without (apo, green, PDB: 6OHW) or with a sialoglycan (Sia, brown, PDB: 6NZK). **d**, Zoom into the NTD from the closed spike (**b**) with the e1 loop (residues 30–38) highlighted in yellow. Dashed lines indicate hydrogen bonds. **e**, Zoom into the contact region between pDPEP1 and the closed spike upon superposition of the RBD-DPEP1 crystal structure on RBD$_A$. DPEP1 is shown with transparent surface to facilitate the identification of the indicated secondary structure elements. Glycans from DPEP1 are shown in wheat, with the one attached to N57 penetrating the spike. Glycans from the spike protomer B are indicated in black sticks. The region where DPEP1 clashes with the spike is highlighted with a wavy red outline. **f**, Fitting of the RBD/pDPEP1 crystal structure into the density map of the open spike. N and C termini are indicated with circled 'N' and 'C' letters, respectively. pDPEP1 is shown with the two RBD molecules found in the asymmetric unit. The viral and cell membranes are drawn to indicate the topology of the complex. This figure was created with BioRender (https://BioRender.com/lv890k6).

(residues 30–38) resembles the HKU1 NTD in its active conformation (Fig. 6c)[7,32]. In this active-like state, the PHEV e1 loop is displaced inwards with respect to the HKU1-apo inactive conformation, T31 contacts W90, P34 interacts with F95, the backbone of S35 forms a hydrogen bond with the N77 backbone amide, S37 main and side chain atoms form hydrogen bonds with F75 backbone, and S38 adopts a protruding position, forming a 'bulge' (Fig. 6d). Overall, these observations indicate that the PHEV spike trimer does not require glycan binding for opening, in contrast to the HKU1 spike and in agreement with our BLI experiments showing that the spike trimer readily binds DPEP1 (Fig. 3g). Finally, to evaluate potential conformational changes upon glycan binding, we incubated the spike trimer with *N*-acetyl-9-*O*-acetylneuraminic acid (9-*O*-acetyl-sialic acid, 9-*O*-Ac-Sia) and analysed it by cryo-EM (Supplementary Fig. 3 and Table 5). Local refinement of neighbouring NTD and RBD from the closed spike produced maps with extra density in the glycan-binding site (Extended Data Fig. 10a), allowing us to model the ligand interacting with canonical residues such as T31, K81, T83 and W90 (Extended Data Fig. 10b)[5,7,32]. Aligning the protomers of the apo and holo closed spikes, or their locally refined NTDs, resulted in CA-RMSDs of 0.86 Å (1,154 atoms and 263 atoms aligned, respectively; Extended Data Fig. 10c), indicating that 9-*O*-Ac-Sia binding does not lead to inter- or intradomain rotations, as observed in the holo HKU1 spike[7,32]. Following incubation with 9-*O*-Ac-Sia, the PHEV spike adopted all of the above-described conformations including closed, 1-RBD-up, 2-RBD-up and open, but with a higher proportion of open forms (Supplementary Fig. 3 and Extended Data Fig. 10d).

DPEP1 binds only open spikes

Finally, to understand whether spike opening is required for DPEP1 binding, we superimposed the RBD/pDPEP1 crystal structure onto the closed spike (Fig. 6f) and evaluated the potential interaction of the receptor with down-RBDs on the trimer. This exercise showed that pDPEP1 cannot bind to a closed spike (for example, to $\mathrm{RBD_A}$) because its α_b-α_1 loop and the glycan attached to N57 in pDPEP1 would clash with the counterclockwise down-RBD from a neighbouring protomer ($\mathrm{RBD_B}$; Fig. 6f and Extended Data Fig. 7). Further steric hindrance could be generated by the spike glycans at N198 and N662, which would lie below pDPEP1 (Fig. 6f). We therefore conclude that DPEP1 can bind only to RBDs in the 'up' position and that the receptor stabilizes open forms of the spike. Moreover, fitting the crystal structure of the RBD–pDPEP1 complex into the cryo-EM density map of the open spikes further shows that the two protomers of the pDPEP1 dimer cannot be reached by the RBDs of a single spike (Fig. 6g), indicating potential linkage of the spikes by the dimeric receptor, as recently shown for SARS-CoV-2 (ref. 36).

Discussion

PHEV circulates subclinically in most swine herds worldwide but causes gastrointestinal and neurologic symptoms in immunologically naive animals, being typically fatal in piglets less than 3–4 weeks of age[37]. Therefore, in the absence of a vaccine or treatment, PHEV poses an economic threat to swine herds. The identification of DPEP1 as a functional PHEV receptor may facilitate the development of new antivirals targeting entry. Previous work showed the involvement of attachment factors in viral entry, including 9-*O*-acetylated sialic acids, heparan sulfates, the neural cell adhesion molecule (NCAM) and the MERS-CoV receptor DPP4 (refs. 8,38–40), but bona fide proteinaceous receptors were unknown for PHEV.

In humans, the main function of DPEP1 is to hydrolyse several dipeptides in renal metabolism. To our knowledge, DPEP1 has not been involved previously in viral infections. In pigs, DPEP1 is mainly expressed in the kidney and gastrointestinal tract[41], which is consistent with the gastrointestinal symptomatology of PHEV infection. However, DPEP1 does not appear to be highly expressed in the pig brain, despite the fact that PHEV is also neurotropic[41]. Low DPEP1 expression in the brain may be sufficient to allow infection, or PHEV could use a different receptor in brain cells. Of the five other genes whose expression correlated with PHEV infectivity in the NCI-60 panel, four are expressed in the pig brain[41]. Investigating whether they may also function as PHEV receptors warrants further study.

Although viruses from the same species usually use the same receptor for viral entry, our study shows that DPEP1 is specific to the PHEV spike. Diversity in receptor usage among members of the betacoronavirus 1 species is probably related to the complex evolutionary history of coronaviruses, which combines a high mutation rate, extensive recombination, frequent host jumps and host adaptation. Importantly, how DPEP1 usage was acquired by PHEV during evolution of the betacoronavirus 1 species remains an open question. PHEV may have acquired its RBD following recombination with an unknown virus or rapid divergence through accumulation of positively selected mutations. We were unable to identify a clear candidate for the origin of the PHEV RBD. Therefore, more work, including novel virus discovery, is needed to understand how and when PHEV acquired DPEP1 usage.

Although betacoronavirus 1 members are host specific, we found that the PHEV spike is compatible with human DPEP1. In contrast, other DPEP1 orthologues did not allow PHEV entry (for example, European hare). The extent of cross-species compatibility of the PHEV spike with mammalian DPEP1 proteins needs to be further explored, as this would help to assess the cross-species transmission potential of PHEV. Indeed, despite widespread subclinical circulation of PHEV in pig farms, its ability to infect other mammals, including humans, remains unclear. In particular, whether PHEV causes asymptomatic infections that go undetected, or whether immunological or post-entry barriers prevent its replication in non-pig hosts, remains to be determined.

Our results argue against a conserved entry mechanism for all embecoviruses. For instance, despite preserving the HE-coding gene, sialic acid promotes but is not required for PHEV entry, in clear contrast with HKU1, OC43 and BCoV. This may be due to the ability of the PHEV spike to adopt open and active conformations even in the absence of a glycan ligand. Specifically, the e1 loop could adopt a conformation primed for conversion to the RBD-up form in the apo state of the PHEV spike. Nevertheless, further stabilization could be achieved by binding a sialoglycan, as evidenced by the increased proportion of RBD-up forms upon incubation with 9-*O*-Ac-Sia. A less prominent role for glycan binding is consistent with studies reporting that the PHEV spike has 1,450- and 45-fold lower affinity for sialoglycans compared with those of BCoV and OC43, respectively[8]. Besides, the higher frequency of RBD opening in the apo state may compensate for the low affinity of the PHEV RBD for DPEP1. We hence propose that, instead of the HKU1 two-step entry mechanism, PHEV follows a model similar to that of SARS-CoV-2, in which a protein receptor binds to spontaneously 'up' RBDs. Nevertheless, our work reveals a conserved binding mode among RBDs from embecoviruses, despite the observed diversity in RBD sequences and receptor specificity. The structural organization of the RBD confers it a remarkable versatility in receptor binding, whereby different sequence motifs can be accommodated into the tip, enabling changes in receptor usage. In particular, the observed insertions/deletions at the tip of the betacoronavirus 1 RBD may be responsible for the receptor usage diversity within this species.

In sum, we have identified a new coronavirus receptor and shown that embecoviruses have divergent mechanisms to regulate the opening of the spike protein, yet they use the RBD tip to recognize different receptors. This parallels the ability of other betacoronaviruses such as sarbeco- and merbecoviruses to adapt a common RBD scaffold to different receptors. Embecoviruses seem to have achieved such versatility by exchanging only small pieces that are confined to the RBD tip, as opposed to the larger variable region observed in other betacoronaviruses.

Methods

Cell lines

The NCI-60 panel was obtained from the National Cancer Institute. The panel consists of 60 well-characterized cancer cell lines from various origins. A total of 48 adherent cell lines were included in our analysis. Their identity was confirmed by short tandem repeat (STR) genotyping, as previously described[18]. NCI-60 cell lines were cultured in RPMI medium (Gibco) supplemented with 10% FBS (Gibco), 10 units $\mathrm{ml^{-1}}$ penicillin, 10 μg $\mathrm{ml^{-1}}$ streptomycin (Gibco), 250 ng $\mathrm{ml^{-1}}$

amphotericin B (Gibco) and 5 µg ml^{-1} prophylactic plasmocin (InvivoGen). HEK293T-GFP1-10 and HEK293T-GFP11 cells were kindly provided by Olivier Schwartz (Institut Pasteur, Paris, France) and were cultured in DMEM medium supplemented with 10% fetal bovine serum (FBS), 1% non-essential amino acids, 10 U ml^{-1} penicillin, 10 µg ml^{-1} streptomycin, 250 ng ml^{-1} amphotericin B and 1 µg ml^{-1} of puromycin (Gibco). PK-15 (Cytion, 607426) and swine primary kidney cells (generated in-house by the National Veterinary Services Laboratories (NVSL), US Department of Agriculture (USDA), Ames, IA, USA) were cultured in MEM (Gibco) supplemented with 10% FBS, 10 U ml^{-1} penicillin, 10 µg ml^{-1} streptomycin and 250 ng ml^{-1} amphotericin B. All cell lines were grown at 37 °C and 5% CO$_2$, and were regularly shown to be free of mycoplasma contamination by PCR.

Plasmids

The genes encoding the full PHEV (GenBank DQ011855.1), OC43 (RefSeq NC_006213.1), BCoV (RefSeq NC_003045.1), ECoV (GenBank EF446615.1), CRCoV (GenBank EU983106.1), HKU24 (RefSeq NC_026011.1), SARS-CoV-2 (RefSeq YP_009724390.1) and MERS-CoV (RefSeq YP_009047204.1) spikes were codon optimized for human expression, synthesized and cloned into a pcDNA3.1 vector bearing a C-terminal 6×His tag (Genscript). The HKU1 spike-encoding plasmid was described previously[42]. To obtain the human DPEP1 (also called human renal dipeptidase, RefSeq NM_001389466.1 with the rs1126464 single nucleotide polymorphism) and TMPRSS2 (RefSeq NM_005656.4) coding sequences, total RNA was extracted from HEK293T or SW-620 cells, respectively, reverse-transcribed using Oligo(dT) and Superscript IV (Invitrogen), amplified by PCR using Phusion Hot Start II DNA polymerase (Thermo Scientific) with specific primers (hDPEP1: 5′-ttaaacttaagcttgccaccatgtggagcggatggtggctg-3′; 5′-tcgtcgtcatccttgtaatccaggagagacagacagaggacc-3′; hTMPRSS2: 5′-ttaaacttaagcttgccaccatggctttgaactcaggg-3′, 5′-tcgtcgtcatccttgtaatcgccgtctgccctcatttg-3′) and cloned into a pcDNA3.1-Flag vector using the NEBuilder HiFi DNA Assembly kit (New England Biolabs) following manufacturer instructions. The pig (*S. scrofa*, RefSeq NM_214108.1), hare (*L. europaeus*, RefSeq XM_062176926.1), cattle (*B. taurus*, RefSeq NM_001034472.2) and dog (*C. lupus*, RefSeq XM_536748.7) orthologues of DPEP1 were synthesized and cloned into a pcDNA3.1-Flag vector (Genscript). pDPEP1, haDPEP1 and PHEV spike mutants were obtained by site-directed mutagenesis using the QuikChange II XL Site-Directed Mutagenesis kit (Agilent) according to manufacturer instructions. Mutagenesis primers are listed in Supplementary Table 6. Successful mutagenesis was confirmed by whole plasmid sequencing (Plasmidsaurus or Eurofins).

Phylogenetic analysis of embecovirus spikes

Multiple sequence alignments of embecovirus spike proteins were performed using the Clustal omega tool in Molecular Evolutionary Genetics Analysis Version 11 (MEGA11) software with default parameters[43]. Evolutionary history was inferred using the maximum-likelihood method and the JTT matrix-based model[44]. The tree with the highest log likelihood is shown. Initial tree(s) for the heuristic search were obtained automatically by applying neighbour-joining and BioNJ algorithms to a matrix of pairwise distances estimated using the JTT model, and then selecting the topology with superior log likelihood value. The tree was drawn to scale, with branch lengths measured by the number of substitutions per site. Bootstrap analysis was used to test the robustness of the tree topology (100 resamplings). Spike protein similarity plots were built using the SimPlot++ software[45], with a 100-amino-acid sliding window and a 10-amino-acid step.

VSV pseudotyping

T75 flasks were coated with poly-D-lysine (Gibco) for 2 h at 37 °C, washed with water and seeded with 8 × 10^6 HEK293T cells. The following day, cells were transfected with 30 µg of plasmid encoding for PHEV S, VSV-G or an empty vector using Lipofectamine 2000 (Invitrogen) following manufacturer instructions. At 24 h post transfection, cells were inoculated at a multiplicity of infection (MOI) of 3 infectious units per cell for 1 h at 37 °C with a VSV encoding GFP, lacking the glycoprotein gene G (VSVΔG-GFP) and previously pseudotyped with G. Cells were washed three times with PBS, and 8 ml of DMEM supplemented with 2% FBS were added. Supernatants containing pseudotypes were collected 24 h later, cleared by centrifugation at 2,000 *g* for 10 min, passed through a 0.45-µm filter, aliquoted and stored at −80 °C.

Infection of the NCI-60 panel

Cells were seeded in 96-well plates the day before the infection. Pseudotypes were mixed 1:1 with an anti-VSV-G monoclonal antibody to remove residual VSV-G and incubated for 20 min at 37 °C. Cell culture medium was removed and cells were inoculated with 50 µl of the antibody-treated pseudotypes. Plates were incubated for 2 h at 37 °C and 50 µl of RPMI medium supplemented with 5% FBS were added to each well. After 20 h, cells were imaged in the Incucyte SX5 Live-Cell Analysis System (Sartorius). The infected cell percentage was calculated as the ratio between cell confluence and the percentage of GFP-positive area, both quantified automatically with the Incucyte Analysis software. Cells were also infected with a bald pseudotype to measure the background signal resulting from cell auto-fluorescence or residual VSV-G-pseudotyped particles. The values obtained in these negative controls were subtracted from the corresponding PHEV pseudotype measurements. All corrected infection values below 0.1% were set to 0.1% (infectivity threshold).

Gene correlation analyses

We normalized infectivity data as previously described[18]. The proportion of infected cells, Q, was measured as the ratio between the GFP area and cell confluence. We transformed Q-values into MOIs as follows: $\text{MOI} = -\ln(1-Q)$. Relative MOI values were then calculated as $R = 100 \times \text{MOI}/\max(\text{MOI})$. Finally, values were log transformed as $\log_2(R+1)$, and the two $\log_2(R+1)$ data obtained in each experimental replicate were averaged. Processed RNA-seq and microarray datasets were downloaded from the CellMiner website (discover.nci.nih.gov/cellminer/loadDownload.do, 'RNA-seq - composite expression' and 'Agilent mRNA - log2' files). These transcriptomic data were available for all cell lines except MDA-MB-468. RNA-sequencing data were available as $\log_2$(rpkm+1) and microarray data as $\log_2$(intensity values). For each gene, RNA-seq and microarray data were first separately scaled as a percentage of the maximal expression value observed among the 47 cell lines. For each cell line–gene combination, scaled RNA-seq and microarray data were then averaged. The average expression data of each gene encoding a membrane-associated protein (7,694 genes) was correlated to $\log_2(R+1)$ infectivity data across the 47 cell lines using Pearson correlation. Bonferroni multiple test correction was applied to identify genes whose expression correlated significantly with infection levels.

Cell–cell fusion assay

The cell–cell fusion assay was performed as previously described[46]. Briefly, HEK293T-GFP1-10 and HEK293T-GFP-11 were mixed at a 1:1 ratio (total of 6 × 10^4 cells per well of a 96-well plate) and were co-transfected with PHEV spike and DPEP1 expression plasmids (or empty vectors) at a 1:1 ratio (100 ng total DNA) using Lipofectamine 2000 (Invitrogen) following manufacturer instructions. For the TMPRSS2 assays, cells were transfected with spike, hDPEP1 and hTMPRSS2 expression plasmids (or empty vectors) at a 1:1:1 ratio (100 ng of total DNA). Plates were placed at 37 °C and 5% CO$_2$ in an Incucyte SX5 Live-Cell Analysis System (Sartorius). GFP signal and phase contrast images were analysed at 18–24 h post transfection. The percentage of fusion was calculated as the ratio between GFP area and cell confluence, both quantified automatically with the Incucyte Analysis software.

CRISPR-Cas9 DPEP1 knockout

Obtention of HCT-15-Cas9 cells. To produce Cas9-encoding lentiviral vectors, 10^6 HEK293T cells were plated in each well of a 6-well plate and transfected 24 h later with a 1:1:1 mix (2.5 µg total DNA) of Cas9-encoding pXPR111 (Addgene, 96924), Gag-Pol-encoding psPAX2 (Addgene, 12260) and VSV-G-encoding pMD2.G (Addgene, 12259) using Lipofectamine 3000 (Invitrogen) following manufacturer instructions. Lentiviral preparations were collected at 48 h post transfection, cleared by centrifugation at 2,000 *g* for 10 min, aliquoted and stored at −80 °C. HCT-15 cells were seeded in poly-D-lysine-coated 12-well plates and spinoculated the next day at 1,000 *g* for 2 h at 30 °C with a 1:5 dilution of the Cas9-encoding lentiviral vector in the presence of 10 µg ml^{-1} polybrene. The following day, cells were washed once with PBS and fresh RPMI supplemented with 10% FBS was added. At 48 h post infection, blasticidin (5 µg ml^{-1}) was added to select Cas9-expressing cells for at least 7 days.

Obtention of DPEP1-KO HCT-15-Cas9 cells. Guide RNAs (gRNAs) against *DPEP1* (#1: 5′-AGAACAAAGACGCCGTGCGG-3′; #2: 5′-CCAAACTGCTGTCAATGGAG-3′) were designed using the CRISPick software[47]. gRNA-coding oligonucleotides were annealed and ligated into BsmBI-digested pRDA-118 vector (Addgene, 133459). To produce gRNA-encoding lentiviral vectors, 10^6 HEK293T cells were plated per well of a 6-well plate and transfected 24 h later with a 1:1:1 mix (2.5 µg total DNA) of pRDA-118-gRNA, Gag-Pol-encoding psPAX2 (Addgene, 12260) and VSV-G-encoding pMD2.G (Addgene, 12259) using Lipofectamine 3000 (Invitrogen) following manufacturer instructions. Lentiviral preparations were collected at 48 h post transfection, cleared by centrifugation at 2,000 *g* for 10 min, aliquoted and stored at −80 °C. HCT-15-Cas9 cells were spinoculated as described above with a 1:5 dilution of the gRNA-encoding lentiviral vectors. At 48 h post infection, puromycin (10 µg ml^{-1}) was added to select gRNA-expressing cells for at least 7 days. Gene KO was confirmed by Sanger sequencing of PCR-amplified genomic DNA and Tracking of Indels by Decomposition analysis[48].

Inhibition of cysteine and serin proteases

HCT-15 cells were pretreated with 100 µM of camostat mesylate (serine protease inhibitor; Sigma-Aldrich), E-64d (cysteine protease inhibitor; Sigma-Aldrich) or vehicle controls for 1 h at 37 °C. Cells were then infected with PHEV pseudotypes as described above. After 20 h, cells were imaged in the Incucyte SX5 Live-Cell Analysis System (Sartorius). The percentage of inhibition was calculated as 100 × (GFP area with vehicle − GFP area with inhibitor)/(GFP area with vehicle). Negative inhibition percentages were set to zero.

Neuraminidase treatment

HCT-15 cells (for PHEV pseudotypes) or TMPRSS2-transfected HEK293T cells (for HKU1 pseudotypes) were plated in a 96-well plate in the presence or absence of 40 µg ml^{-1} of neuraminidase (NA) from *Clostridium perfringens* (Sigma-Aldrich). The next day, cells were infected with PHEV, HKU1 or VSV-G pseudotypes as described above, in the presence or absence of 40 µg ml^{-1} NA. Cells were also infected with a GFP-expressing influenza A virus (IAV, strain PR8) as a positive control for sialic acids depletion. After 18–24 h, cells were imaged in the Incucyte SX5 Live-Cell Analysis System (Sartorius). The infected cell percentage was calculated as the ratio between cell confluence and the percentage of GFP-positive area, both quantified automatically with the Incucyte Analysis software.

Pseudotype infectivity competition assay

PHEV pseudotypes were pre-incubated 1:1 with anti-VSV-G antibody and with serial dilutions of soluble hDPEP1 (Sino Biologicals) or vehicle (H_2O) for 1 h at 37 °C, and then used to infect either HCT-15 or hDPEP1-transfected HEK293T cells seeded the previous day in 96-well plates. The percentage of infected cells at 18–24 h post infection was measured using the Incucyte SX5 Live-Cell Analysis System (Sartorious) and the Incucyte Analysis software.

Flow cytometry measurement of hDPEP1 binding

HEK293T cells were seeded in 6-well plates. The next day, they were transfected with 2.5 µg of spike-encoding plasmid using Lipofectamine 2000 following manufacturer instructions. After 24 h, cells were detached gently with cold staining buffer (PBS, 0.5% BSA, 2 mM EDTA) and incubated with serial dilutions of soluble recombinant hDPEP1 (Sino Biologicals) for 30 min at 4 °C. Cells were washed with PBS and incubated with an anti-DPEP1 antibody (Atlas Antibodies, HPA012783, dilution 1:100) for 30 min at 4 °C. After another wash with PBS, cells were incubated with a goat anti-rabbit IgG-AF647 secondary antibody (Invitrogen, A32733, dilution 1:400) for 30 min at 4 °C. Cells were fixed with 4% paraformaldehyde for 10 min at room temperature, washed with PBS and resuspended in staining buffer. Cells were analysed on a FACSVerse (BD Biosciences) flow cytometer and results were analysed using the FlowJo software (v.10.10). The median fluorescence intensity (MFI) obtained at each soluble hDPEP1 concentration was normalized to the one obtained in the absence of soluble hDPEP1.

Full virus competition assay

PHEV (strain 67N) was obtained from the NVSL, USDA and was propagated in swine kidney primary cells (SPKC) as previously described[49]. For the competition assay, SPKC and PK-15 cells were plated in a 12-well plate. The next day, the virus was incubated with soluble hDPEP1 (Sino Biologicals) or vehicle (H_2O) at a concentration of 25 µg ml^{-1} for 30 min at 37 °C. Cells were then inoculated with 100 µl of treated virus and incubated for 2 h at 37 °C. Cells were washed three times with PBS and 1 ml of MEM supplemented with 2% FBS was added. Supernatants were collected at 2, 12, 24 and 48 h post-inoculation and viral RNA was extracted using the NZY Viral RNA Isolation kit (NZYtech) according to manufacturer instructions. Viral RNA (PHEV N) was quantified by RT–qPCR using previously published primers and probe[50], and the *Taq*Path 1-Step RT–qPCR Master Mix (Applied Biosystems) according to manufacturer instructions.

Western blot

A 1-ml volume of supernatant containing pseudotype was pelleted by centrifugation at 30,000 *g* for 2 h at 4 °C and lysed in 30 µl of NP-40 lysis buffer (Invitrogen) for 30 min on ice. Around 5×10^5 transfected cells were lysed in 50 µl of NP-40 lysis buffer (Invitrogen) for 30 min on ice. Lysates were cleared by centrifugation at 15,000 *g* for 10 min at 4 °C. Cleared lysates were mixed with 4× Laemlli buffer (Bio-Rad) supplemented with 10% β-mercaptoethanol and denatured at 95 °C for 5 min. Proteins were separated by SDS–PAGE on a 4–20% Mini-PROTEAN TGX Gel (Bio-Rad) and transferred onto a 0.45 µm PVDF membrane (Thermo Scientific). Membranes were blocked for 1 h at room temperature in TBS-T (20 mM Tris, 150 mM NaCl, 0.1% Tween-20, pH 7.5) supplemented with 3% BSA (Sigma). Membranes were then incubated for 1 h at room temperature with the following primary antibodies: mouse anti-His-Tag (dilution 1:1,000, clone HIS.H8, Invitrogen, MA121315), mouse anti-Flag (dilution 1:1,000, clone M2, Sigma-Aldrich, F1804), mouse anti-VSV-M (dilution 1:1,000, clone 23H12, Kerafast, EB0011) and rabbit anti-GAPDH (dilution 1:3,000, Sigma-Aldrich, ABS16). Membranes were washed 3 times with TBS-T and incubated for 1 h at room temperature with an HRP-conjugated anti-mouse (dilution 1:50,000, Invitrogen, G-21040) or anti-rabbit (dilution 1:50,000, Invitrogen, G-21234) secondary antibody. After 3 washes in TBS-T, the signal was revealed with SuperSignal West Pico PLUS (Thermo Scientific) following manufacturer instructions. Images were acquired on an ImageQuant LAS 500 (GE Healthcare) and analysed with Fiji software. Uncropped western blot images are provided as Source Data files.

Construct design for protein expression and purification

Codon-optimized synthetic genes coding for the PHEV spike (residues 15–1,274, GenBank AAY68297.1), pDPEP1 (residues 17–385, GenBank CAA37762.1, UniProt P22412) and SARS-CoV-2 Omicron BA.4/5 spike[51] (residues 1–1,208, Wuhan numbering) were purchased from Genscript. Cloning of these genes was also performed by Genscript. hDPEP1 (residues 17–385) was amplified from the plasmid used for functional assays described above and Q351 was mutated to E351, matching the Uniprot sequence P16444. Plasmids coding for the SARS-CoV-2 Wuhan RBD and soluble ACE2 have been previously described[14].The PHEV-spike ectodomain was stabilized in the prefusion form by introducing mutations in the furin site (^{751}RSRR^{754} to ^{751}GSAG^{754}) and adding a Foldon (YIPEAPRDGQAYVRKDGEWVLLSTFL) trimerization motif at the C terminus. This construct was cloned into pCAGGS with an Ig kappa signal peptide (METDTLLLWVLLLWVPGSTG) and a thrombin cleavage site at the C terminus (LVPRGS) followed by His- (HHHHHHHH), Strep- (WSHPQFEK) and Avi tags (GLNDIFEAQKIEWHE). This plasmid was used as a template to amplify the PHEV RBD (residues 327–605) coding sequence, which was cloned into pCAGGs with the same signal peptide and tags as the spike. The SARS-CoV-2 Omicron BA.4/5 spike ectodomain was stabilized with six proline mutations in S2 (equivalent to F817P, A892P, A899P, A942P, K986P and V987P, Wuhan numbering), the abrogation of furin cleavage (^{682}RRAR^{685} to ^{682}GSAS^{685}, Wuhan numbering) and the addition of a C-terminal Foldon motif. This construct was cloned in the pCI-Neo plasmid, followed by His, Strep and Avi tags.

Soluble pDPEP1 was cloned into a modified pcDNA3.1(+) vector, which contains a CMV exon-intron-exon sequence to boost expression, downstream of the CD5 signal peptide (MPMGSLQPLATLYLLGMLVASCLG) and upstream of an enterokinase cleavage site (DDDDK) and a double Strep tag. pDPEP1 and hDPEP1 constructs (DPEP1-Avi) were designed with a single Strep sequence followed by the Avi tag after the enterokinase site.

For expression in insect cells, the PHEV RBD and pDPEP1 were cloned into a modified pMT/BiP plasmid (Invitrogen; hereafter termed pT350), which translates the protein in frame with an enterokinase cleavage site and a double strep tag at the C-terminal end.

Protein expression and purification

Protein expression and purification for X-ray crystallography. Plasmids encoding the PHEV RBD or pDPEP1 were co-transfected with the pCoPuro plasmid for puromycin selection in *Drosophila* Schneider line 2 cells (S2) using the Effectene transfection reagent (Qiagen). The cell lines underwent selection in serum-free insect cell medium (HyClone, Cytiva) containing 7 µg ml^{-1} puromycin and 1% penicillin/streptomycin. For protein production, the cells were grown in spinner flasks until the density reached 10^7 cells per ml, at which point the protein expression was induced with 4 µM $CdCl_2$. After 6 days, the cultures were centrifuged, and the supernatants were concentrated and used for affinity purification in a Strep-Tactin column (IBA). The strep tags were removed by incubating the proteins with 48–60 units of Enterokinase light chain (BioLabs) in the elution buffer supplemented with 2 mM $CaCl_2$, at room temperature, overnight. The proteolysis reactions were buffer exchanged into 10 mM Tris, 100 mM NaCl, pH 8.0 and subjected to a second affinity purification, recovering the flow-through fraction containing the untagged proteins. The proteins were concentrated and the enzymatic deglycosylation with endoglycosidase D (EndoD, 500 units) and endoglycosidase H (EndoH, 1,000 units) was set up at room temperature following overnight incubation in 50 mM Na acetate, 200 mM NaCl, pH 5.0. The proteins were further purified on a size exclusion chromatography (SEC) Superdex 200 16/600 (Cytiva) column in 10 mM Tris, 100 mM NaCl, pH 8.0 and concentrated in VivaSpin concentrators. The purity of the final protein samples was analysed by SDS–PAGE followed by Coomasie blue staining.

Purification of complexes used for crystallization screenings. The PHEV RBD was incubated with pDPEP1 (after enterokinase cleavage and deglycosylation) at final concentrations of 150 µM and 42.3 µM (dimer), respectively. Following overnight incubation at 4 °C, the reaction was loaded onto a Superdex 200 10/300 increase column (Cytiva) equilibrated in 10 mM Tris-HCl and 100 mM NaCl (pH 8.0) to isolate the complex by SEC. Eluted fractions were analysed by SDS–PAGE and those corresponding to the complex were pooled, concentrated to 8.8 mg ml^{-1} and used in crystallization trials.

Protein expression and purification for biophysical assays and cryo-EM. pDPEP1, pDPEP1-Avi, hDPEP1-Avi, ACE2, PHEV RBD, SARS-CoV-2 RBD, PHEV-spike and SARS-CoV-2 spike ectodomain-encoding plasmids were transiently transfected into Expi293F cells (Thermo Fisher, A14527) using FectoPro DNA transfection reagent (PolyPlus). After 5 days at 37 °C, cells were collected by centrifugation and proteins from the supernatants were purified by affinity chromatography in a Strep-Tactin column (IBA). The eluted fractions were pooled, concentrated and loaded onto a Superdex 200 10/300 increase column (Cytiva) (RBDs, DPEP1, ACE2) or a Superose 6 10/300 increase column (Cytiva) (spikes) that had been previously equilibrated in 10 mM Tris-HCl and 100 mM NaCl (pH 8.0). Fractions from each main peak were concentrated and frozen. The purity of the final protein samples was analysed by SDS–PAGE followed by Coomasie blue staining.

Crystallization and structural determination

Crystallization screening trials were carried out by the vapour diffusion method using a Mosquito nanodispensing system (STPLabtech) following established protocols[52]. The best crystals of the PHEV RBD–pDPEP1 complex were obtained in 0.1 M 2-(*N*-morpholino)ethanesulfonic acid (MES, pH 6.0), 0.2 M zinc acetate and 10% w/v polyethylene glycol (PEG) 8000 at 18 °C using the sitting-drop vapour diffusion method. Crystals were flash frozen by immersion into a cryo-protectant containing the crystallization solution supplemented with 33% (v/v) ethylene glycol (EG), followed by rapid transfer into liquid nitrogen. The X-ray diffraction data were collected at 100 K at the Proxima 2A beamline of the SOLEIL synchrotron source (Saint Aubin, France)[53]. Data were processed, scaled and reduced with XDS[54] and AIMLESS[55]. The structures were determined by molecular replacement using Phaser from the PHENIX suite[56], with search ensembles obtained from AlphaFold3 (ref. 26) (PHEV RBD) and the crystal structure of hDPEP1 (PDB: 1ITQ). The final models were built by combining real-space model building in Coot[57] with reciprocal space refinement with phenix.refine. The final model was validated with Molprobity[58]. The analyses of the macromolecular surfaces were carried out in PDBePISA[59]. Figures were created using Pymol[60], Chimera[61] and BioRender.com.

Sample preparation for cryo-EM

Of the PHEV-spike ectodomain (0.6 µM trimer), 3 µl were added to Quantifoil R1.2/1.3 200 mesh copper grids (Delta microscopies), which had been glow discharged twice using a Pelco glow discharge system at 15 mA for 25 s. Samples were vitrified in 100% liquid ethane using a Mark IV Vitrobot (Thermo Fisher) by blotting for 3.5 s with Whatman No. 1 filter paper at 8 °C and 100% relative humidity, after a 15-s waiting time. To evaluate the effect of sialic acid binding, the PHEV-spike ectodomain (0.7 µM trimer) was incubated with 1 mM *N*-acetyl-9-*O*-acetylneuraminic acid (TCI, A3414, CAS: 55717-54-9) for 1 h at room temperature and then used to prepare the grids as indicated before.

Cryo-EM data collection, processing, refinement and modelling

Data collection was performed on a Glacios transmission electron microscope (Thermo Fisher) operating at 200 kV, using the EPU automated image acquisition software (Thermo Fisher). Movies were collected on a Falcon 4i direct electron detector operating in counted mode at a nominal magnification of ×240,000 (0.58 Å per pixel) using a defocus range of −0.75 to −2.5 µm. Movies were collected over a 1.8-s exposure and a total dose of ~40 e^{-} Å^{-2}. The data processing workflows are summarized in Supplementary Figs. 2 and 3. Briefly, all movies were motion corrected and dose weighted with MotionCorr2 (ref. 62), and the aligned micrographs were used to estimate the defocus values with patchCTF within cryoSPARC[63]. CryoSPARC blob picker was used for automated particle picking. The resulting particles were extracted (binning 4, 2.32 Å per pixel) and used to obtain initial two-dimensional (2D) classes. The classes without clear features or with poor alignment were discarded, and the remaining particles were re-extracted (binning 2, 1.16 Å per pixel) and used for a new round of 2D classification. Then, three ab initio 3D models were generated in CryoSPARC, followed by heterogeneous refinement. The particles from the best class were subjected to CryoSPARC 3D classification into 10 classes without initial volumes or masks. The maps from the different classes were analysed to assign them a conformation (closed, 1-RBD-up, 2-RBD-up, open, or unidentifiable). Particles from the classes corresponding to the same conformational state were submitted to non-uniform refinement in CryoSPARC (C3 symmetry applied to the 'closed' and 'open' conformation maps)[64]. The final maps were sharpened with DeepEMhancer[65] and the local resolution was estimated in CryoSPARC. Structural details on the NTD were obtained using masks encompassing neighbouring RBD and NTD (closed forms of apo and holo spike), or the NTD alone (open holo spike). Particles from the non-uniform refinement maps were used for symmetry expansion (C3), particle subtraction and local refinement in CryoSPARC. The final maps were sharpened with DeepEMhancer[65] and the local resolution was estimated in CryoSPARC. Model building of the NTD started with an AlphaFold3 model of the trimeric full-length spike (ipTM: 0.82; pTM: 0.82), from which the NTD was isolated, and the crystal structure of the RBD. They were fitted into the EM map of the locally refined closed apo state using UCSF Chimera. Then, a molecular dynamics flexible fitting followed by real-space refinement was performed with the Namdinator tool[66]. After that, iterative rounds of manual building and real-space and B-factor refinement in Coot and Phenix[56] were performed, using secondary structure restraints. The atomic model of the spike protomer was built on the basis of the AlphaFold3 prediction, where the RBD and NTD were replaced by those resulting from the previous step. As before, the protomer was submitted to flexible fitting on Namdinator and iterative rounds of manual building and real-space and B-factor refinement in Coot and Phenix[56]. Then, symmetry operators were obtained from the EM map with the map-symmetry tool from Phenix, and they were used to place the three copies of the protomer within the trimeric map with the apply-NCS-operators Phenix tool. A final round of real-space refinement was performed in Phenix. The models of the holo-states were built from the apo structures, which were fitted into the maps with UCSF Chimera, and submitted to flexible fitting on Namdinator and iterative rounds of manual building and real-space and B-factor refinement in Coot and Phenix[56]. Validation of model coordinates was performed using MolProbity.

BLI

The affinity of recombinant proteins was assessed in real time using a biolayer interferometry Octet-R8 device (Sartorius). Initial binding experiments were performed by loading nickel-nitriloacetic acid (Ni-NTA) capture sensors (Sartorius) for 10 min at 1,000 r.p.m. shaking speed with the PHEV RBD at 200 nM (or the SARS-CoV-2 RBD at 100 nM) in PBS. The sensors were then blocked with PBS containing BSA at 1.0 mg ml^{-1} (assay buffer) and incubated at 1,000 r.p.m. with 2-fold serially diluted concentrations (500 nM to 15.6 nM) of pDPEP1 (or hACE2) in assay buffer. Association and dissociation were monitored for 240 s and 180 s, respectively. A sample reference measurement was recorded from a sensor loaded with each RBD and dipped in the assay buffer. Specific signals were calculated by subtracting non-specific signals obtained for the sample reference from the signals recorded for the RBD-loaded sensors dipped in pDPEP1 (or hACE2) solutions. Two independent experiments were performed but only the curves obtained at 500 nM in the first experiment were chosen for Fig. 3. Experiments to evaluate binding of the PHEV spike were performed with pDPEP1-Avi. This protein was biotinylated with a kit (Avidity) following manufacturer instructions, and the reaction buffer was exchanged to PBS. Biotinylated pDPEP1-Avi (50 nM dimer) was immobilized on streptavidin capture sensors (Sartorius) for 10 min at 1,000 r.p.m. shaking speed. The sensors were then blocked with assay buffer and incubated with 2-fold serially diluted concentrations (100 nM to 3.125 nM) of PHEV spike (or Omicron BA.4/5 spike used as a control) in assay buffer. Association and dissociation were monitored for 240 s. A sample reference measurement was recorded from a sensor loaded with pDPEP1-Avi and dipped in the assay buffer. After each dissociation step, the sensors were regenerated by dipping them for 30 s in 10 mM acetate buffer (pH 4.0) and 30 s in PBS (three times). Affinity of the recombinant PHEV RBD towards pDPEP1 and hDPEP1 was determined following a similar protocol. Streptavidin capture sensors (Sartorius) were loaded for 10 min at 1,000 r.p.m. shaking speed with biotinylated pDPEP1-Avi at 50 nM (dimer) in PBS. The sensors were then blocked with assay buffer, and incubated at 1,000 r.p.m. with 2-fold serially diluted concentrations (starting at 8, 6 or 4 µM) of PHEV RBD in assay buffer. Association and dissociation were monitored for 240 s. A sample reference measurement was recorded from a sensor loaded with pDPEP1-Avi and dipped in the assay buffer. Regeneration steps were performed with 10 mM acetate buffer (pH 4.0) as indicated before. The steady-state signal was plotted against the analyte concentration, and the curve was fitted assuming a 1:1 binding model. Six (pDPEP1) or three (hDPEP1) independent experiments were performed and the dissociation constant (K_d) values from each of them were averaged and used to calculate the standard deviation.

Statistics and reproducibility

Statistics were performed in GraphPad Prism v.10. All details about statistical tests can be found in the figure legends or in the main text. No statistical method was used to predetermine sample size. No data were excluded from the analyses. The experiments were not randomized. The investigators were not blinded to allocation during experiments and outcome assessment.

Biosafety

All viruses were handled under BSL-2 conditions at the facilities of the Institute for Integrative Systems Biology. The procedures were approved by the Biosafety Committee of the Universitat de València (protocol 3389116) and by the Comisión Nacional de Bioseguridad of the Spanish Ministerio de Agricultura, Pesca y Alimentación (authorizations A/ES/22/72 and A/ES/24/92).

Reporting summary

Further information on research design is available in the Nature Portfolio Reporting Summary linked to this article.

Data availability

All data supporting the findings of this study are available in this Article. The following structures have been deposited in the Protein Data Bank (PDB) with the accession codes indicated in parentheses: PHEV RBD–pDPEP1 complex (9H0B), closed apo PHEV spike trimer (9H3J), locally refined NTD-RBD from the closed apo spike (9R6O), closed PHEV spike trimer with 9-O-Ac-Sia (9R6P), locally refined NTD-RBD from the closed holo spike (9R6Q) and locally refined NTD of the open holo PHEV spike (9R6R). The cryo-EM maps have been deposited in the Electron Microscopy Data Bank (EMDB) under accession codes: EMD-51827 (closed apo PHEV spike), EMD-51844 (1-RBD-up apo PHEV spike), EMD-51845 (2-RBD-up apo PHEV spike), EMD-51846 (open apo PHEV spike), EMD-53679 (locally refined map of the NTD-RBD from the closed apo spike), EMD-53680 (closed holo PHEV spike), EMD-53681 (1-RBD-up holo PHEV spike), EMD-53682 (2-RBD-up holo PHEV spike), EMD-53683 (open holo PHEV spike), EMD-53684 (locally refined map of the NTD-RBD from the closed holo spike) and EMD-53685 (locally refined map of the NTD from the open holo spike). Source data are provided with this paper.

References

1. Cui, J., Li, F. & Shi, Z. L. Origin and evolution of pathogenic coronaviruses. *Nat. Rev. Microbiol.* **1717**, 181–192 (2018).
2. Vijgen, L. et al. Complete genomic sequence of human coronavirus OC43: molecular clock analysis suggests a relatively recent zoonotic coronavirus transmission event. *J. Virol.* **79**, 1595–1604 (2005).
3. Hulswit, R. J. G., de Haan, C. A. M. & Bosch, B. J. Coronavirus spike protein and tropism changes. *Adv. Virus Res.* **96**, 29–57 (2016).
4. Walls, A. C. et al. Cryo-electron microscopy structure of a coronavirus spike glycoprotein trimer. *Nature* **531**, 114–117 (2016).
5. Tortorici, M. A. et al. Structural basis for human coronavirus attachment to sialic acid receptors. *Nat. Struct. Mol. Biol.* **26**, 481–489 (2019).
6. Kirchdoerfer, R. N. et al. Pre-fusion structure of a human coronavirus spike protein. *Nature* **531**, 118–121 (2016).
7. Pronker, M. F. et al. Sialoglycan binding triggers spike opening in a human coronavirus. *Nature* https://doi.org/10.1038/s41586-023-06599-z (2023).
8. Hulswit, R. J. G. et al. Human coronaviruses OC43 and HKU1 bind to 9-*O*-acetylated sialic acids via a conserved receptor-binding site in spike protein domain A. *Proc. Natl Acad. Sci. USA* **116**, 2681–2690 (2019).
9. Vlasak, R., Luytjes, W., Spaan, W. & Palese, P. Human and bovine coronaviruses recognize sialic acid-containing receptors similar to those of influenza C viruses. *Proc. Natl Acad. Sci. USA* **85**, 4526–4529 (1988).
10. Wang, M. & Veit, M. Hemagglutinin-esterase-fusion (HEF) protein of influenza C virus. *Protein Cell* **7**, 28–45 (2016).
11. Rosenthal, P. B. et al. Structure of the haemagglutinin-esterase-fusion glycoprotein of influenza C virus. *Nature* **396**, 92–96 (1998).
12. Huang, X. et al. Human coronavirus HKU1 spike protein uses *O*-acetylated sialic acid as an attachment receptor determinant and employs hemagglutinin-esterase protein as a receptor-destroying enzyme. *J. Virol.* **89**, 7202–7213 (2015).
13. Li, Z. et al. Synthetic *O*-acetylated sialosides facilitate functional receptor identification for human respiratory viruses. *Nat. Chem.* **13**, 496–503 (2021).
14. Saunders, N. et al. TMPRSS2 is a functional receptor for human coronavirus HKU1. *Nature* **624**, 207–214 (2023).
15. Fernández, I. et al. Structural basis of TMPRSS2 zymogen activation and recognition by the HKU1 seasonal coronavirus. *Cell* **187**, 4246–4260.e16 (2024).
16. McCallum, M. et al. Human coronavirus HKU1 recognition of the TMPRSS2 host receptor. *Cell* **187**, 4231–4245.e13 (2024).
17. Wang, H. et al. TMPRSS2 and glycan receptors synergistically facilitate coronavirus entry. *Cell* **187**, 4261–4271.e17 (2024).
18. Dufloo, J., Andreu-Moreno, I., Moreno-Garcia, J., Valero-Rello, A. & Sanjuán, R. Receptor-binding proteins from animal viruses are broadly compatible with human cell entry factors. *Nat. Microbiol.* **10**, 405–419 (2025).
19. Reinhold, W. C. et al. RNA sequencing of the NCI-60: integration into CellMiner and CellMiner CDB. *Cancer Res.* **79**, 3514–3524 (2019).
20. Liu, H. et al. mRNA and microRNA expression profiles of the NCI-60 integrated with drug activities. *Mol. Cancer Ther.* **9**, 1080–1091 (2010).
21. Wang, L. & Tian, G. Insight into dipeptidase 1: structure, function, and mechanism in gastrointestinal cancer diseases. *Transl. Cancer Res.* **13**, 7015–7025 (2024).
22. Choudhury, S. R. et al. Dipeptidase-1 is an adhesion receptor for neutrophil recruitment in lungs and liver. *Cell* **178**, 1205–1221.e17 (2019).
23. Hoffmann, M. et al. SARS-CoV-2 cell entry depends on ACE2 and TMPRSS2 and is blocked by a clinically proven protease inhibitor. *Cell* **181**, 271–280.e8 (2020).
24. Iwata-Yoshikawa, N. et al. TMPRSS2 contributes to virus spread and immunopathology in the airways of murine models after coronavirus infection. *J. Virol.* https://doi.org/10.1128/JVI.01815-18 (2019).
25. Kaminski, K., Ludwiczak, J., Pawlicki, K., Alva, V. & Dunin-Horkawicz, S. pLM-BLAST: distant homology detection based on direct comparison of sequence representations from protein language models. *Bioinformatics* https://doi.org/10.1093/bioinformatics/btad579 (2023).
26. Abramson, J. et al. Accurate structure prediction of biomolecular interactions with AlphaFold 3. *Nature* **630**, 493–500 (2024).
27. Nitanai, Y., Satow, Y., Adachi, H. & Tsujimoto, M. Crystal structure of human renal dipeptidase involved in β-lactam hydrolysis. *J. Mol. Biol.* **321**, 177–184 (2002).
28. Adair, A. et al. Human coronavirus OC43 nanobody neutralizes virus and protects mice from infection. *J. Virol.* https://doi.org/10.1128/jvi.00531-24 (2024).
29. Shang, J. et al. Structure of mouse coronavirus spike protein complexed with receptor reveals mechanism for viral entry. *PLoS Pathog.* **16**, e1008392 (2020).
30. Ou, X. et al. Crystal structure of the receptor binding domain of the spike glycoprotein of human betacoronavirus HKU1. *Nat. Commun.* **8**, 15216 (2017).
31. Holm, L., Laiho, A., Törönen, P. & Salgado, M. DALI shines a light on remote homologs: one hundred discoveries. *Protein Sci.* https://doi.org/10.1002/pro.4519 (2023).
32. Jin, M. et al. Human coronavirus HKU1 spike structures reveal the basis for sialoglycan specificity and carbohydrate-promoted conformational changes. *Nat. Commun.* **16**, 4158 (2025).
33. Frank, S. et al. Stabilization of short collagen-like triple helices by protein engineering. *J. Mol. Biol.* **308**, 1081–1089 (2001).
34. Hsieh, C.-L. et al. Structure-based design of prefusion-stabilized SARS-CoV-2 spikes. *Science* **369**, 1501–1505 (2020).
35. Pallesen, J. et al. Immunogenicity and structures of a rationally designed prefusion MERS-CoV spike antigen. *Proc. Natl Acad. Sci. USA* https://doi.org/10.1073/pnas.1707304114 (2017).
36. Grunst, M. W. et al. Structure and inhibition of SARS-CoV-2 spike refolding in membranes. *Science* **385**, 757–765 (2024).
37. Mora-Díaz, J. C., Piñeyro, P. E., Houston, E., Zimmerman, J. & Giménez-Lirola, L. G. Porcine hemagglutinating encephalomyelitis virus: a review. *Front. Vet. Sci.* **6**, 435768 (2019).
38. Gao, W. et al. Identification of NCAM that interacts with the PHE-CoV spike protein. *Virol. J.* **7**, 254 (2010).
39. Dong, B. et al. A small region of porcine hemagglutinating encephalomyelitis virus spike protein interacts with the neural cell adhesion molecule. *Intervirology* **58**, 130–137 (2015).
40. Shi, J. et al. Dipeptidyl peptidase 4 interacts with porcine coronavirus PHEV spikes and mediates host range expansion. *J. Virol.* https://doi.org/10.1128/jvi.00753-24 (2024).
41. Karlsson, M. et al. Genome-wide annotation of protein-coding genes in pig. *BMC Biol.* **20**, 25 (2022).

42. Cantoni, D. et al. Analysis of antibody neutralisation activity against SARS-CoV-2 variants and seasonal human coronaviruses NL63, HKU1, and 229E induced by three different COVID-19 vaccine platforms. *Vaccines* **11**, 58 (2023).
43. Tamura, K., Stecher, G. & Kumar, S. MEGA11: Molecular Evolutionary Genetics Analysis Version 11. *Mol. Biol. Evol.* **38**, 3022–3027 (2021).
44. Jones, D.T., Taylor, W.R. & Thornton, J.M. The rapid generation of mutation data matrices from protein sequences. *Bioinformatics* **8**, 275–282 (1992).
45. Samson, S., Lord, É. & Makarenkov, V. SimPlot++: a Python application for representing sequence similarity and detecting recombination. *Bioinformatics* **38**, 3118–3120 (2022).
46. Buchrieser, J. et al. Syncytia formation by SARS-CoV-2-infected cells. *EMBO J.* **39**, e106267 (2020).
47. Doench, J. G. et al. Optimized sgRNA design to maximize activity and minimize off-target effects of CRISPR-Cas9. *Nat. Biotechnol.* **34**, 184–191 (2016).
48. Brinkman, E. K., Chen, T., Amendola, M. & van Steensel, B. Easy quantitative assessment of genome editing by sequence trace decomposition. *Nucleic Acids Res.* https://doi.org/10.1093/NAR/GKU936 (2014).
49. Nelli, R. K., Mora-Díaz, J. C.& Giménez-Lirola, L. G. The betacoronavirus PHEV replicates and disrupts the respiratory epithelia and upregulates key pattern recognition receptor genes and downstream mediators, including IL-8 and IFN-λ. *mSphere* **6**, e0082021 (2021).
50. Hu, X. et al. Development of a quadruplex real-time quantitative RT-PCR for detection and differentiation of PHEV, PRV, CSFV, and JEV. *Front. Vet. Sci.* https://doi.org/10.3389/FVETS.2023.1276505 (2023).
51. Tegally, H. et al. Emergence of SARS-CoV-2 Omicron lineages BA.4 and BA.5 in South Africa. *Nat. Med.* **28**, 1785–1790 (2022).
52. Weber, P. et al. High-throughput crystallization pipeline at the crystallography core facility of the Institut Pasteur. *Molecules* **24**, 4451 (2019).
53. Chavas, L. M. G. et al. PROXIMA-1 beamline for macromolecular crystallography measurements at Synchrotron SOLEIL. *J. Synchrotron Radiat.* **28**, 970–976 (2021).
54. Kabsch, W. Integration, scaling, space-group assignment and post-refinement. *Acta Crystallogr. D. Biol. Crystallogr.* **66**, 133–144 (2010).
55. Evans, P. R. & Murshudov, G. N. How good are my data and what is the resolution? *Acta Crystallogr. D Biol. Crystallogr.* **69**, 1204–1214 (2013).
56. Liebschner, D. et al. Macromolecular structure determination using X-rays, neutrons and electrons: recent developments in Phenix. *Acta Crystallogr. D Struct. Biol.* **75**, 861–877 (2019).
57. Emsley, P., Lohkamp, B., Scott, W. G. & Cowtan, K. Features and development of *Coot*. *Acta Crystallogr. D Biol. Crystallogr.* **66**, 486–501 (2010).
58. Williams, C. J. et al. MolProbity: more and better reference data for improved all-atom structure validation. *Protein Sci.* **27**, 293–315 (2018).
59. Krissinel, E. & Henrick, K. Inference of macromolecular assemblies from crystalline state. *J. Mol. Biol.* **372**, 774–797 (2007).
60. Schrödinger LLC. *The PyMOL Molecular Graphics System* Version 1.8 (2015).
61. Pettersen, E. F. et al. UCSF Chimera—a visualization system for exploratory research and analysis. *J. Comput. Chem.* **25**, 1605–1612 (2004).
62. Zheng, S. Q. et al. MotionCor2: anisotropic correction of beam-induced motion for improved cryo-electron microscopy. *Nat. Methods* **14**, 331–332 (2017).
63. Punjani, A., Rubinstein, J. L., Fleet, D. J. & Brubaker, M. A. cryoSPARC: algorithms for rapid unsupervised cryo-EM structure determination. *Nat. Methods* **14**, 290–296 (2017).
64. Punjani, A., Zhang, H. & Fleet, D. J. Non-uniform refinement: adaptive regularization improves single-particle cryo-EM reconstruction. *Nat. Methods* **17**, 1214–1221 (2020).
65. Sanchez-Garcia, R. et al. DeepEMhancer: a deep learning solution for cryo-EM volume post-processing. *Commun. Biol.* **4**, 874 (2021).
66. Kidmose, R. T. et al. Namdinator - automatic molecular dynamics flexible fitting of structural models into cryo-EM and crystallography experimental maps. *IUCrJ* **6**, 526–531 (2019).
67. Holm, L. Using Dali for protein structure comparison. *Methods Mol. Biol.* **2112**, 29–42 (2020).

Acknowledgements

We thank the staff of the Crystallography platform at Institut Pasteur and the synchrotron source SOLEIL (Saint Aubin, France) for granting access to the facility; the staff of the beamline Proxima 2A for advice and assistance during X-ray data collections; P. Guardado-Calvo (Institut Pasteur, Paris, France) for access to the Octet-R8; the NanoImaging Core at Institut Pasteur for support with sample preparation, image acquisition and analysis. The NanoImaging Core was created with the help of a grant from the French Government's Investissements d'Avenir programme (EQUIPEX CACSICE - Centre d'analyse de systèmes complexes dans les environnements complexes, ANR-11-EQPX-0008). We thank O. Schwartz (Institut Pasteur, Paris, France) for the GFP-split cells; J. Buigues Bisquert (I2SysBio, Paterna, Spain) and R. Martínez Recio (I2SysBio, Paterna, Spain) for technical assistance. This work was financially supported by an ERC Advanced Grant (101019724–EVADER) and a grant from the Spanish Ministerio de Ciencia e Innovación (PID2020-118602RB-I00–ZooVir) to R.S. J.D. is the recipient of an EMBO postdoctoral fellowship (ALTF-140-2021) and a Marie Skłodowska-Curie Actions Postdoctoral Fellowship (101104880). F.A.R. was funded by ANRS-MIE Project EMERGEN - ANRS 0149 - PRODEVAR and by Labex IBEID (grant ANR-10-LABX-62-IBEID). The funders had no role in study design, data collection and analysis, decision to publish or preparation of the manuscript.

Author contributions

J.D., I.F., F.A.R. and R.S. designed research; J.D., I.F., A.A. and A.H. performed research; J.D., I.F. and R.S. analysed data; J.D., I.F., F.A.R. and R.S. wrote the manuscript; F.A.R. and R.S. provided funding. N.T. and L.G.G.-L. provided essential material. All authors read and approved the final version of the manuscript.

Competing interests

The authors declare no competing interests.

Additional information

Extended data is available for this paper at https://doi.org/10.1038/s41564-025-02111-7.

Supplementary information The online version contains supplementary material available at https://doi.org/10.1038/s41564-025-02111-7.

Correspondence and requests for materials should be addressed to Félix A. Rey or Rafael Sanjuán.

Peer review information *Nature Microbiology* thanks the anonymous reviewers for their contribution to the peer review of this work.

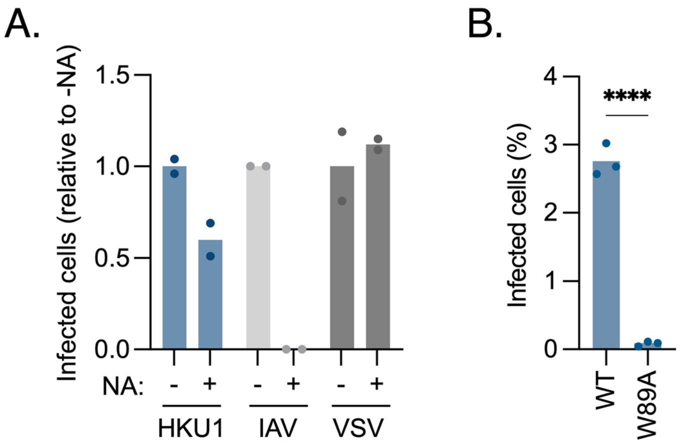

Extended Data Fig. 1 | HKU1 strongly depends on sialic acid for entry. **a**. hTMPRSS2-transfected HEK293T cells were treated or not with neuraminidase and infected with VSV-G and HKU1 VSV pseudotypes or IAV (PR8-GFP). The ratio of infected cells relative to no NA treatment is shown. Each dot represents a technical replicate (n = 2) and the bar represents the mean. **b**. hTMPRSS2-transfected HEK293T cells were infected with a WT or W89A HKU1 pseudotype. The percentage of infected cells is shown. Each dot represents a technical replicate (n = 3) and the bar represents the mean. The level of statistical significance of a two-sided unpaired t-test is shown: **** $P < 0.0001$.

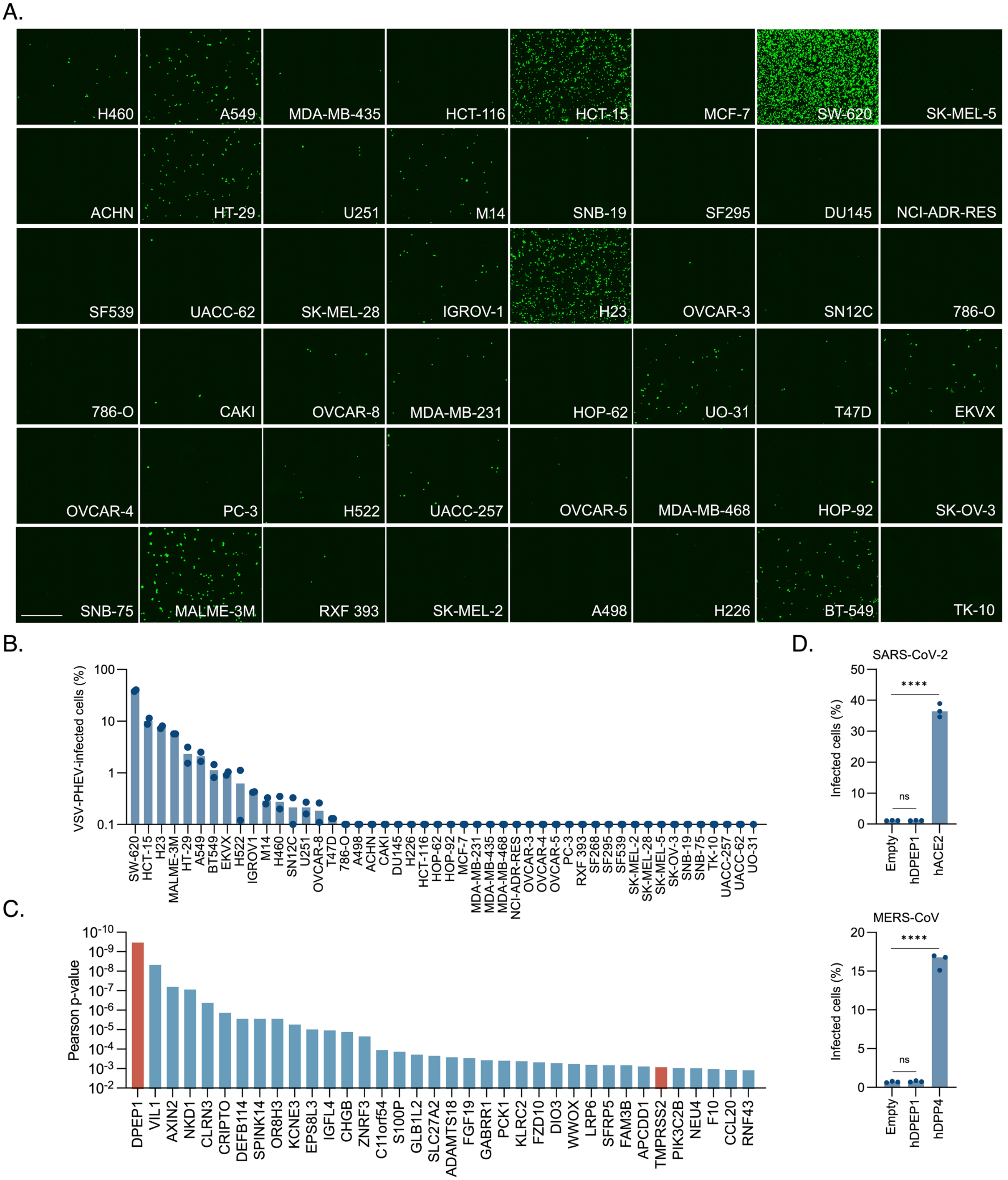

Extended Data Fig. 2 | Infection of the NCI-60 panel with PHEV pseudotypes. **a**. 48 cell lines from the NCI-60 panel were infected with PHEV pseudotypes and imaged 20 h later with the SX5 Live-Cell Analysis System at a 4X magnification. Images show the GFP signal obtained in one of the two independent replicates performed. Cell line abbreviations are shown. Scale bar: 100 µm. **b**. The percentage of infection of VSV-PHEV in the 48 cell lines of the NCI-60 panel is shown. The bar shows the mean and each dot represents an independent experiment (n = 2). **c**. PHEV pseudotype infectivity was correlated with the expression of 7,694 genes expressing membrane-associated proteins. The Pearson correlation p-values of the 40 genes best correlating with infectivity are shown. **d**. HEK293T cells were transfected with hDPEP1, human ACE2 (hACE2). human DPP4 (hDPP4), or an empty vector and infected with SARS-CoV-2 (top) or MERS-CoV (bottom) pseudotypes. The percentage of infected cells is shown. The bar shows the mean, each dot represents a technical replicate (n = 3), and the significance of a two-sided unpaired t-test is indicated. **** $P < 0.0001$, ns not significant ($P = 0.95$ for SARS-CoV-2 and $P = 0.40$ for MERS-CoV).

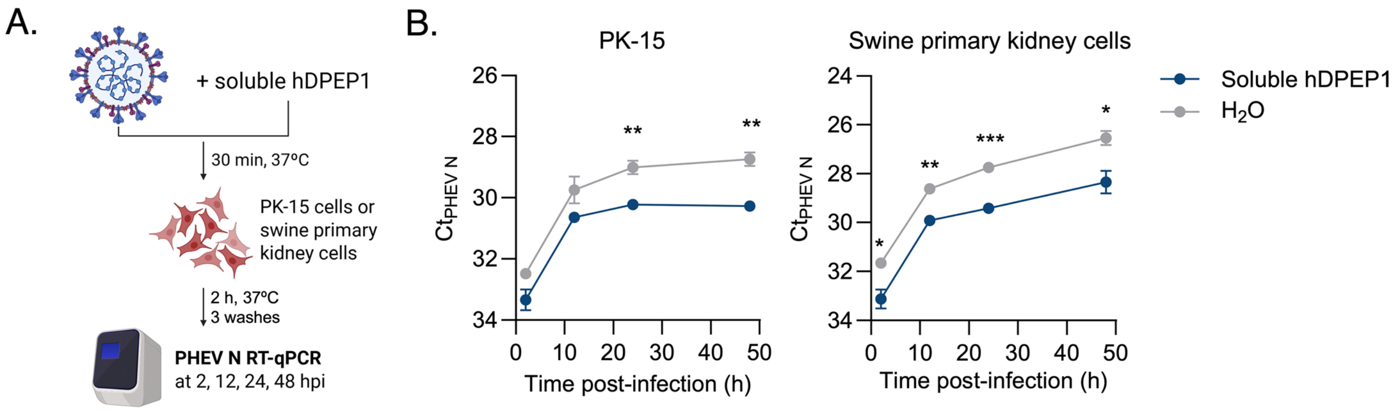

Extended Data Fig. 3 | Soluble DPEP1 inhibits PHEV replication. a. Schematic of the full virus competition assay. Briefly, PHEV was pre-incubated with soluble hDPEP1 and used to infect PK-15 or swine primary kidney cells. Viral input was removed, cells were thoroughly washed with PBS, and viral release was followed by RT-qPCR of the supernatants at several times post-infection. This figure was created in BioRender (https://BioRender.com/cpcvv3w). **b.** PHEV N Ct values at different times post-infection with (blue) or without (grey) soluble hDPEP1. To display results in a more comprehensible way, the y-axis is reversed. Each dot represents the mean ± SEM of three replicates. The Ct values in both treatments (Soluble hDPEP1 vs H2O) were compared at each time point using a two-sided unpaired t-test: * $P < 0.05$; ** $P < 0.01$; *** $P < 0.001$. For PK-15, at 24 h: $P = 0.0053$; 48 h: $P = 0.0031$. For swine primary kidney cells, at 2 h: $P = 0.019$; 12 h: $P = 0.0017$; 24 h: $P = 0.0008$; 48 h: $P = 0.026$.

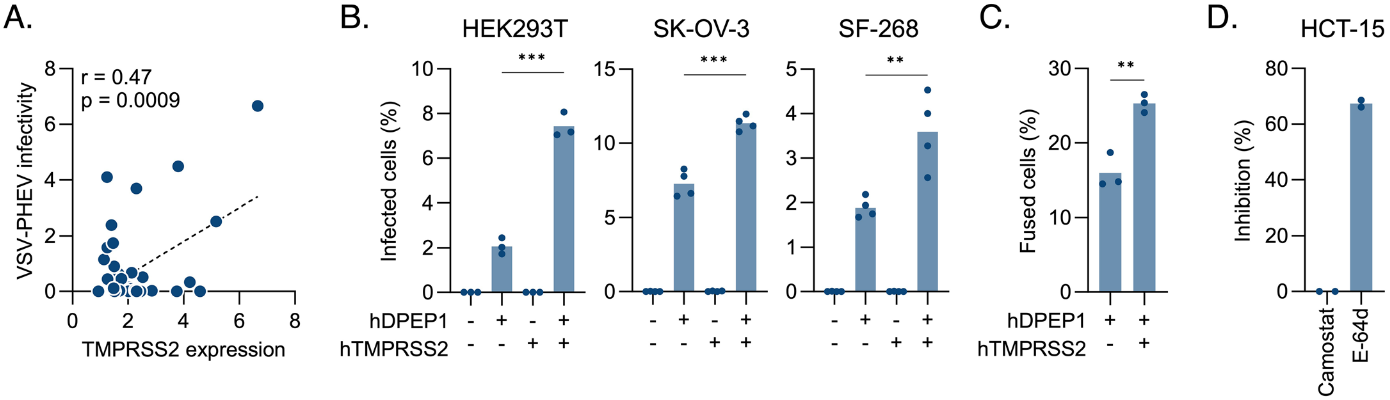

Extended Data Fig. 4 | TMPRSS2 enhances DPEP1-mediated PHEV entry. **a**. Correlation between the expression of TMPRSS2 with the infectivity of PHEV pseudotypes in the NCI-60 cell line panel. Each point corresponds to a different cell line (n = 47). Pearsons r and p-value are indicated. **b**. HEK293T, SK-OV-3 and SF-268 cells were transfected with hDPEP1 and/or hTMPRSS2 (or an empty vector) and infected with PHEV pseudotypes. The percentage of infected cells is shown. **c**. HEK293T GFP-Split cells were transfected with hDPEP1 and hTMPRSS2 or an empty vector. The percentage of cell-cell fusion is shown. **d**. HCT-15 cells were pre-treated with 100 µM camostat mesylate or E-64d prior to infection with PHEV pseudotypes. The data show the percentage of entry inhibition for each inhibitor. Each point represents a technical replicate (n = 2). One representative experiment of three independent replicates is shown. In B and C, the bar shows the mean, each dot represents a technical replicate (n = 3-4) from 1-2 independent experiments, and the significance of a two-sided unpaired t-test is indicated. ** $P < 0.01$; *** $P < 0.005$. In B, for HEK293T cells: $P = 0.0002$; SK-OV-3: $P = 0.0002$; SF-268: $P = 0.0086$. In C, $P = 0.0036$.

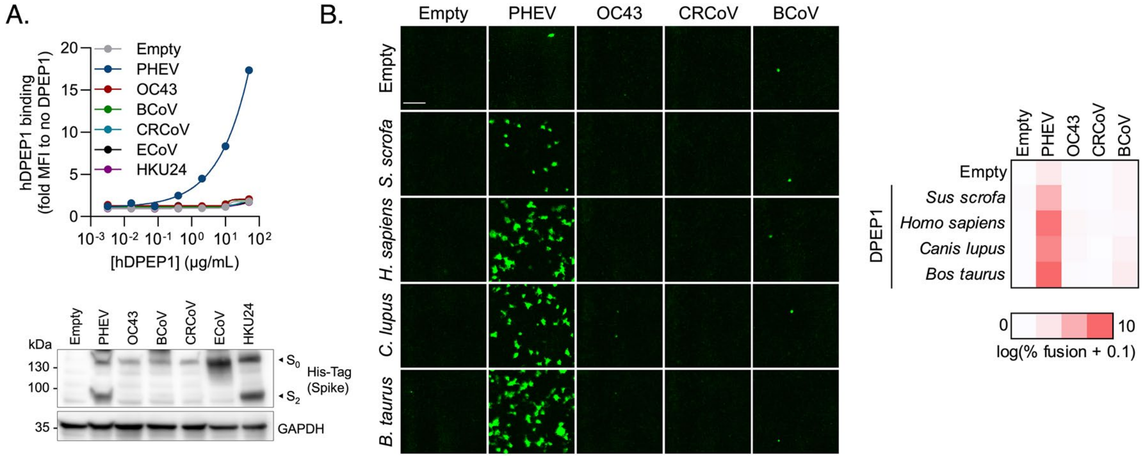

Extended Data Fig. 5 | DPEP1 is a PHEV-specific receptor. a. Flow cytometry measurement of soluble hDPEP1 binding to HEK293T cells transfected with betacoronavirus 1 spikes or an empty vector. Top: the data shows the binding median fluorescence intensity (MFI) measured at each concentration of soluble hDPEP1 normalized to the MFI in the absence of hDPEP1, in cells transfected with an empty vector or the indicated betacoronavirus 1 spike. Results from a representative experiment out of two are shown. Bottom: Western blot confirmation of spike expression. A His-Tag added to the spike C-terminus was used for detection and GAPDH was used as a loading control. **b**. HEK293T GFP-Split cells were transfected with the indicated betacoronavirus 1 spike and DPEP1 ortholog, or an empty vector. Representative images are shown on the left (scale bar: 200 µm). The log-transformed percentage of cell-cell fusion is shown on the right. The mean of three technical replicates is shown (n = 3).

https://doi.org/10.1038/s41564-025-02111-7

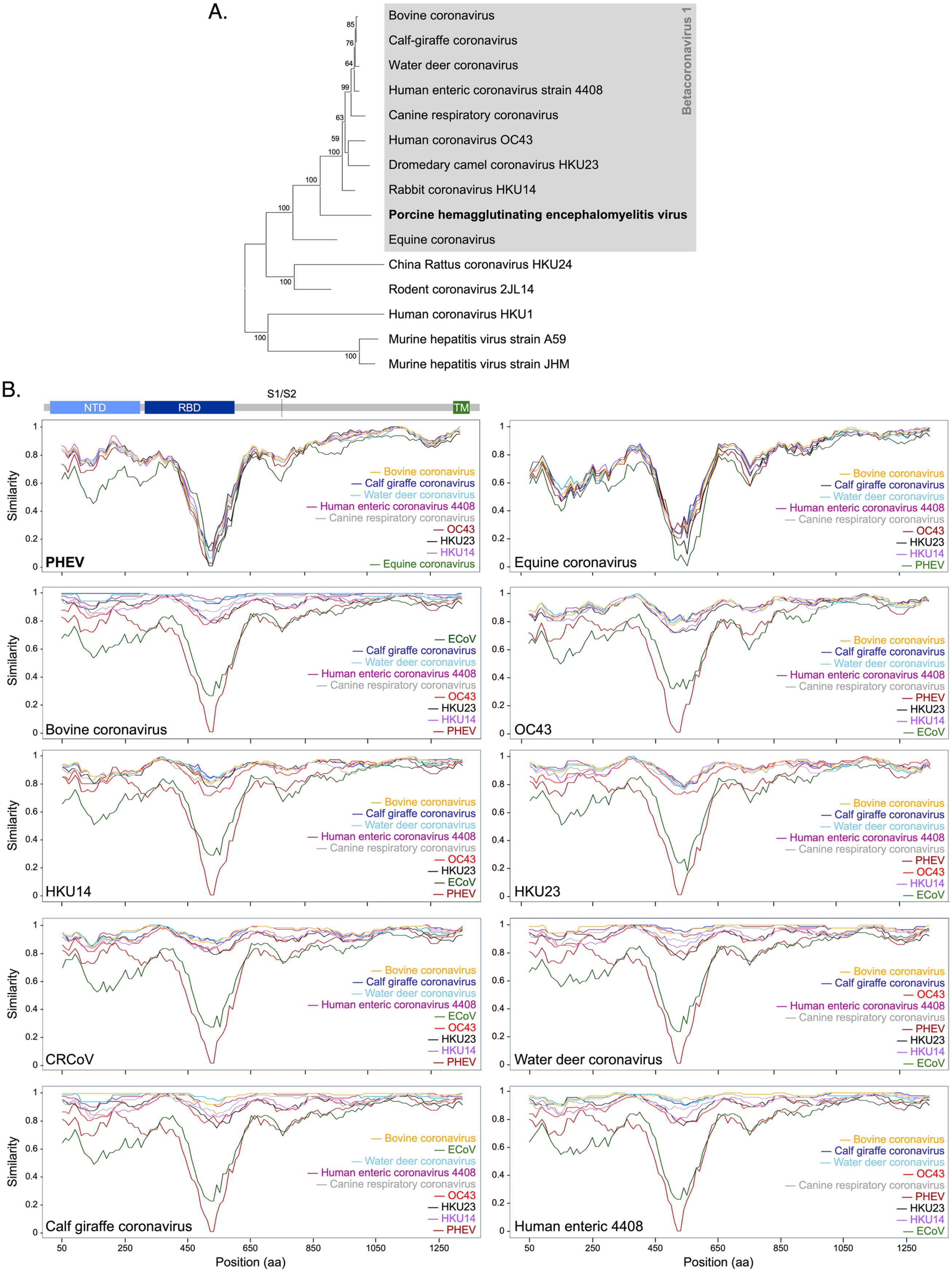

Extended Data Fig. 6 | Diversity of the betacoronavirus 1 spike proteins. a. Maximum-likelihood phylogeny of embecovirus spike proteins. The grey shaded area shows the betacoronavirus 1 members. Bootstrap values of each node are shown. **b.** Similarity plots showing the percentage of similarity between the betacoronavirus 1 spikes. The spike used as a reference is indicated in the bottom-left corner. A schematic of the betacoronavirus 1 spike organization is shown at the top (NTD: N-terminal domain, RBD: receptor-binding domain, TM: transmembrane domain).

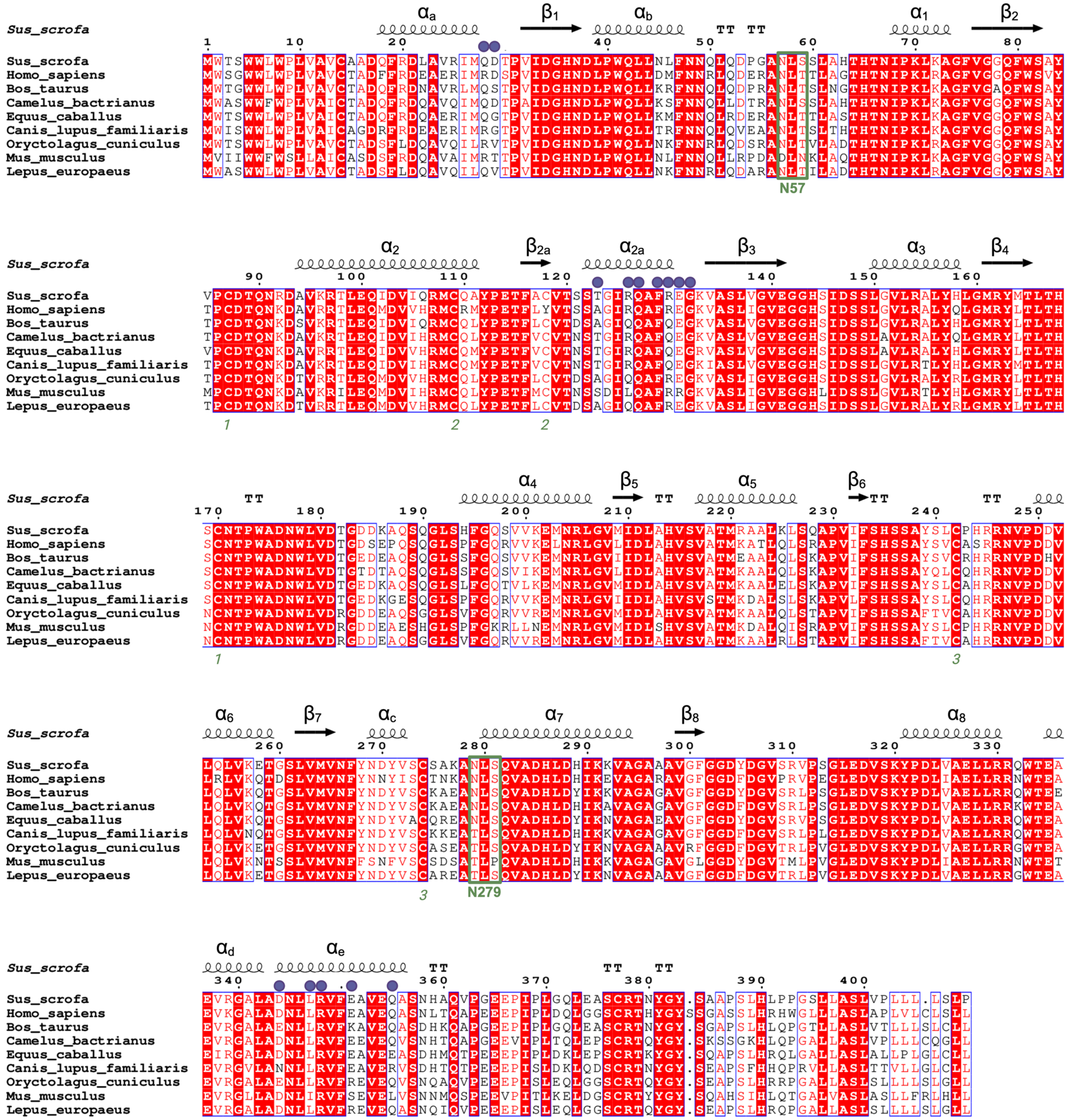

Extended Data Fig. 7 | The PHEV binding determinants on DPEP1 are partially conserved across mammals. Amino acid sequence alignment of DPEP1 from selected mammals, calculated with MUSCLE and rendered with ESPript 3.0. Strictly conserved residues are in a red background and relatively conserved positions in red font. The secondary structure elements are labeled above the alignment. Residues contacted by the PHEV RBD are marked by violet full circles. Cysteines paired in disulfide bonds are indicated by the matching green numbers below the alignment. N-linked glycosylation sites are framed in green with the asparagine residue labeled. The sequences were obtained from the following accession numbers in Uniprot: Sus scrofa: P22412, Homo sapiens: P16444, Bos taurus Q3SZM7, Camelus bactrianus: A0A9W3FLA3, Equus caballus: F6TJM7, Canis lupus familiaris: A0A8P0THL7, Oryctolagus cuniculus: P31429, Mus musculus: P31428, Lepus europaeus: UPI002B47CA68. This figure was created in BioRender (https://BioRender.com/pawqyys).

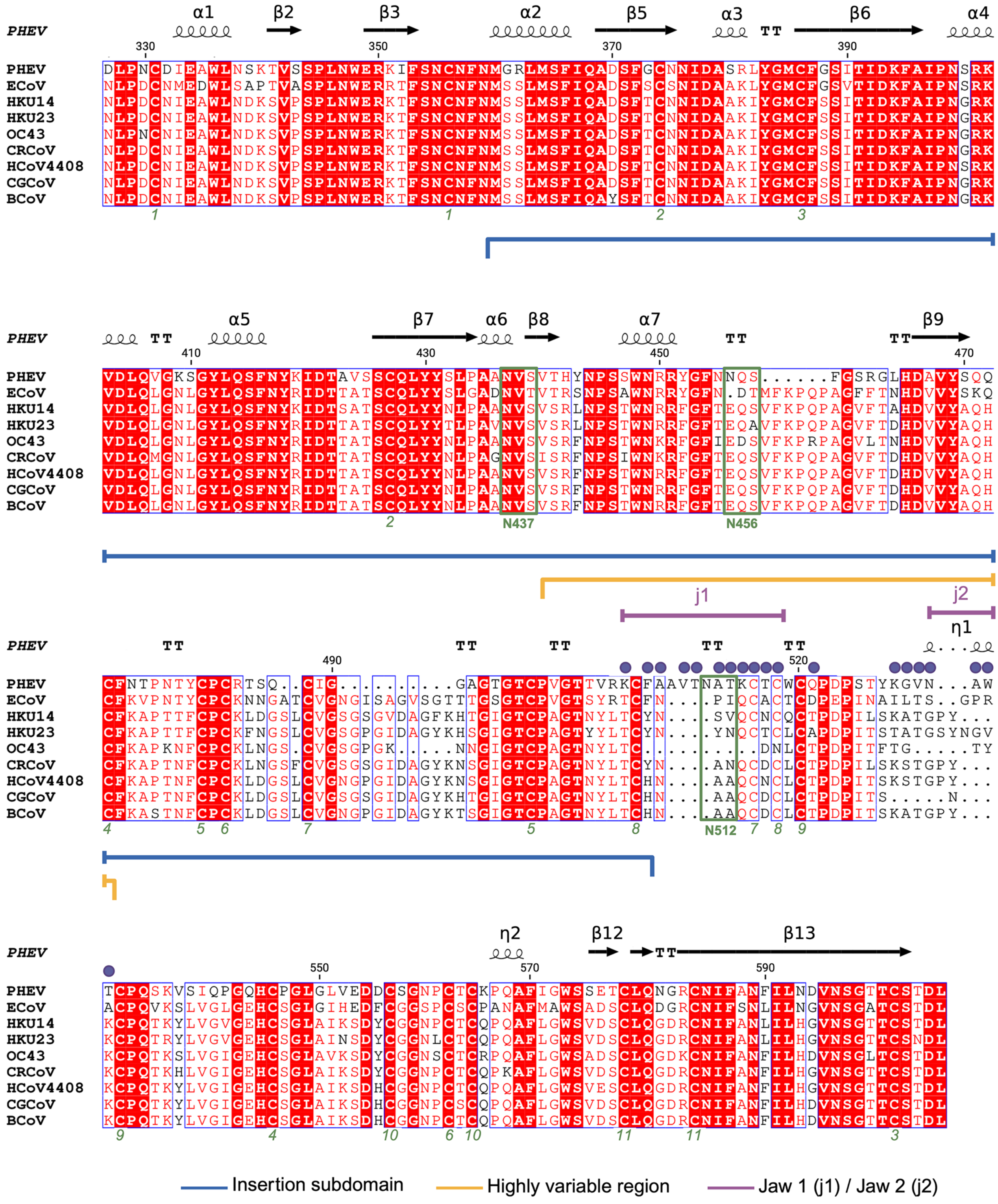

Extended Data Fig. 8 | Variable segments of the RBD recognize DPEP1. Amino acid sequence alignment of the RBD region of the spike of members of the betacoronavirus 1 species, calculated and rendered as in Extended Data Fig. 7, with small black dots indicating gaps. The secondary structure elements observed in the PHEV RBD are labeled above the alignment. The insertion subdomain is indicated with a blue line and the highly variable region by an orange line. Elements j1 and j2 introduced in Fig. 4 are in purple, and residues that contact DPEP1 in the structure are marked by violet full circles. Cysteines paired in disulfide bonds are indicated by the green number below the alignment. The three N-linked glycosylation sites in the PHEV RBD are framed in green (N437 conserved across species, and N412 and N512 specific to PHEV). Note the important deletion in OC43 in the region of j1, which eliminates two cysteine residues involved in two different disulfide bonds. The crystal structure shows that the cysteines involved in disulfide bonds 7 and 8, left without their partner, form a disulfide bond with each other. The sequences used in the alignment have the following NCBI accession numbers: PHEV: AAY68297.1, ECoV: ABP87990.1, HKU14: YP_005454245.1, HKU23: QEY10641.1, OC43: YP_009555241.1, CRCoV: ACL93319.1, HCoV4408: ACT11030.1, CGCoV: ABP38313.1, BCoV: NP_150077.1. This figure was created in BioRender (https://BioRender.com/12mwbzm).

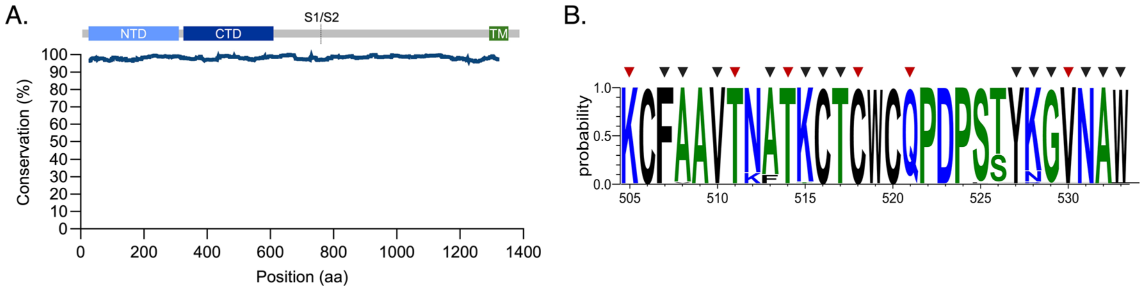

Extended Data Fig. 9 | Conservation of DPEP1-interacting residues across known PHEV strains. a. Percentage of amino acid conservation in the spike of all known PHEV strains (n = 52 sequences). A 50 aa sliding window was used. A schematic of the PHEV spike organization is shown at the top (NTD: N-terminal domain, RBD: receptor-binding domain, TM: transmembrane domain). **b**. Probability of different amino acids occupying the indicated positions (numbers at the bottom) of the spike protein of all known PHEV strains (n = 52 sequences). Inverted triangles indicate the residues involved in the interaction with pDPEP1, with those in red forming polar interactions.

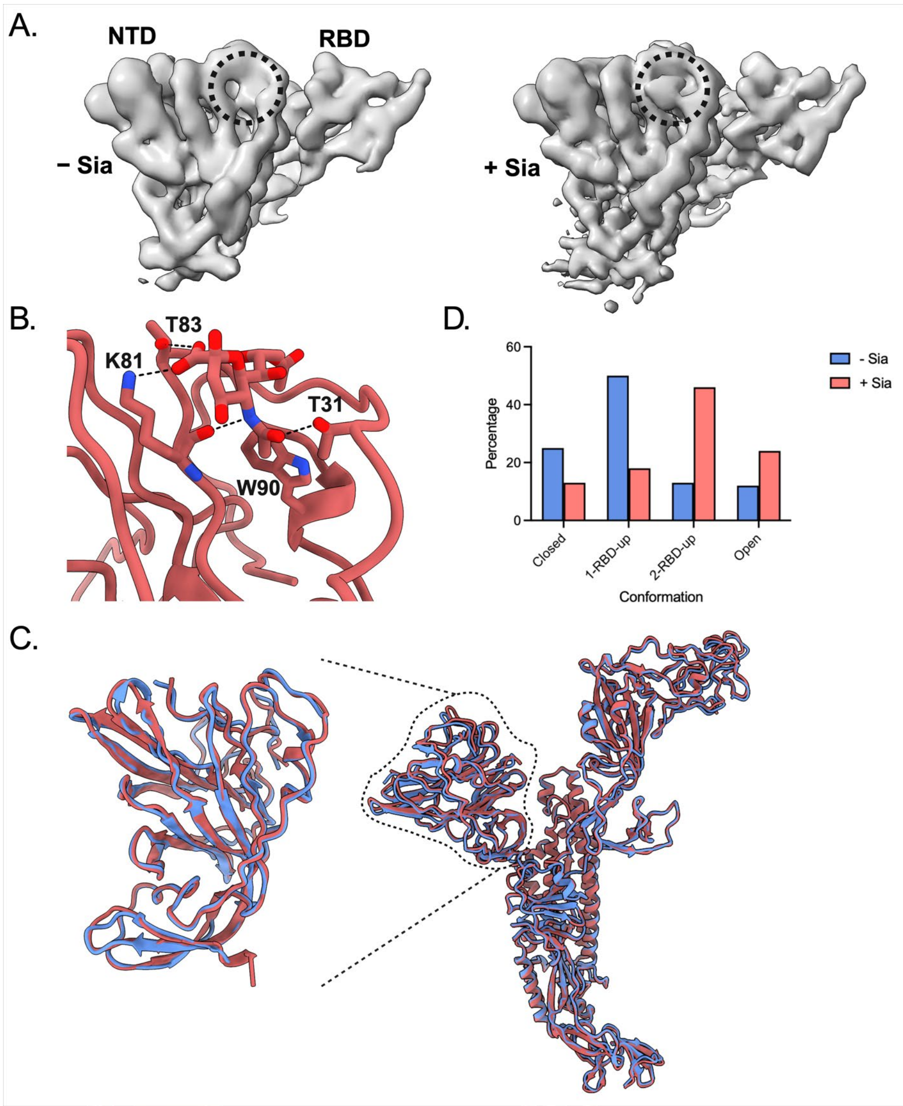

Extended Data Fig. 10 | Cryo-electron microscopy (cryo-EM) of the PHEV spike ectodomain in the presence of 9-O-acetylated sialic acid (9-O-Ac-Sia). a. Density maps of the NTD and the neighboring RBD obtained by local refinement from a spike without ligands (- Sia, left) and incubated with 9-O-Ac-Sia (+ Sia, right). A dashed circle indicates extra density at the conserved glycan binding site that is only observed in the presence of the ligand. **b**. Atomic model of the NTD and 9-O-Ac-Sia. Residues that contact the ligand are labeled and shown in sticks. Dashed lines represent hydrogen bonds. **c**. Superposition of protomers from PHEV closed spikes without a ligand (blue) and incubated with 9-O-Ac-Sia (red). The NTD is outlined with a dashed line and magnified on the left. **d**. Plot indicating the percentage of the different spike conformations obtained upon 3D classification of the spike datasets collected in the absence (-Sia, blue) or presence (+ Sia, red) of 9-O-Ac-Sia. This figure was created in BioRender (https://BioRender.com/ry1m6t5).

nature portfolio

Corresponding author(s): Rafael Sanjuán and Félix Rey
Last updated by author(s): Jul 25, 2025

Reporting Summary

Nature Portfolio wishes to improve the reproducibility of the work that we publish. This form provides structure for consistency and transparency in reporting. For further information on Nature Portfolio policies, see our Editorial Policies and the Editorial Policy Checklist.

Statistics

For all statistical analyses, confirm that the following items are present in the figure legend, table legend, main text, or Methods section.

n/a	Confirmed	
☐	☒	The exact sample size (*n*) for each experimental group/condition, given as a discrete number and unit of measurement
☐	☒	A statement on whether measurements were taken from distinct samples or whether the same sample was measured repeatedly
☐	☒	The statistical test(s) used AND whether they are one- or two-sided *Only common tests should be described solely by name; describe more complex techniques in the Methods section.*
☒	☐	A description of all covariates tested
☐	☒	A description of any assumptions or corrections, such as tests of normality and adjustment for multiple comparisons
☐	☒	A full description of the statistical parameters including central tendency (e.g. means) or other basic estimates (e.g. regression coefficient) AND variation (e.g. standard deviation) or associated estimates of uncertainty (e.g. confidence intervals)
☐	☒	For null hypothesis testing, the test statistic (e.g. *F*, *t*, *r*) with confidence intervals, effect sizes, degrees of freedom and *P* value noted *Give P values as exact values whenever suitable.*
☒	☐	For Bayesian analysis, information on the choice of priors and Markov chain Monte Carlo settings
☒	☐	For hierarchical and complex designs, identification of the appropriate level for tests and full reporting of outcomes
☐	☒	Estimates of effect sizes (e.g. Cohen's *d*, Pearson's *r*), indicating how they were calculated

Our web collection on statistics for biologists contains articles on many of the points above.

Software and code

Policy information about availability of computer code

Data collection	FACSSuite Incucyte software 2022B Rev2 MXCuBE (version 2) EPU (ThermoFisher, version 3.10.0.8733) Octet BLI Discovery 13.0.1.29
Data analysis	Graphpad Prism v10 FlowJo v10.10 Fiji v2.1.0 Microsoft® Excel® for Microsoft 365 MSO (Version 2312 Build 16.0.17126.20132) 64 bits Molecular Evolutionary Genetics Analysis Version 11 (MEGA11) SimPlot++ v1.3 XDS (version January 10, 2022) CCP4 (version 8) Phenix (version 1.21.2-5419) Coot (version 0.9.8.1) CryoSPARC (version 4) Pymol (version 3.0.3) Chimera (version 1.16) ChimeraX (version 1.9) Molprobity (https://molprobity.biochem.duke.edu/)

PDBePISA (https://www.ebi.ac.uk/pdbe/pisa/)
Namdinator (https://namdinator.au.dk/)
Octet Analysis Studio 13.0.1.35

For manuscripts utilizing custom algorithms or software that are central to the research but not yet described in published literature, software must be made available to editors and reviewers. We strongly encourage code deposition in a community repository (e.g. GitHub). See the Nature Portfolio guidelines for submitting code & software for further information.

Data

Policy information about availability of data

All manuscripts must include a data availability statement. This statement should provide the following information, where applicable:

- Accession codes, unique identifiers, or web links for publicly available datasets
- A description of any restrictions on data availability
- For clinical datasets or third party data, please ensure that the statement adheres to our policy

All data supporting the findings of this study are available in this article. The following structures have been deposited to the Protein Data Bank (PDB) with the accession codes indicated between parenthesis: PHEV RBD-pDPEP1 complex (9H0B), closed apo PHEV spike trimer (9H3J), locally refined NTD-RBD from the closed apo spike (9R6O), closed PHEV spike trimer with 9-O-Ac-Sia (9R6P), locally refined NTD-RBD from the closed holo spike (9R6Q), locally refined NTD of the open holo PHEV spike (9R6R). The cryo-EM maps have been deposited to the Electron Microscopy Data Bank (EMDB) under accession codes: EMD-51827 (closed apo PHEV spike), EMD-51844 (1-RBD-up apo PHEV spike), EMD-51845 (2-RBD-up apo PHEV spike), EMD-51846 (open apo PHEV spike), EMD-53679 (locally refined map of the NTD-RBD from the closed apo spike), EMD-53680 (closed holo PHEV spike), EMD-53681 (1-RBD-up holo PHEV spike), EMD-53682 (2-RBD-up holo PHEV spike), EMD-53683 (open holo PHEV spike), EMD-53684 (locally refined map of the NTD-RBD from the closed holo spike), EMD-53685 (locally refined map of the NTD from the open holo spike).

Research involving human participants, their data, or biological material

Policy information about studies with human participants or human data. See also policy information about sex, gender (identity/presentation), and sexual orientation and race, ethnicity and racism.

Reporting on sex and gender	NA
Reporting on race, ethnicity, or other socially relevant groupings	NA
Population characteristics	NA
Recruitment	NA
Ethics oversight	NA

Note that full information on the approval of the study protocol must also be provided in the manuscript.

Field-specific reporting

Please select the one below that is the best fit for your research. If you are not sure, read the appropriate sections before making your selection.

☒ Life sciences ☐ Behavioural & social sciences ☐ Ecological, evolutionary & environmental sciences

For a reference copy of the document with all sections, see nature.com/documents/nr-reporting-summary-flat.pdf

Life sciences study design

All studies must disclose on these points even when the disclosure is negative.

Sample size	No statistical method was used to predetermine sample size. The sample size is indicated in the figure legends and are sufficient for a robust statistical analysis. Performing >2-3 replicates is a standard for in vitro life science studies, in particular in virology since this allows robust statistical analysis of the results.
Data exclusions	No data were excluded.
Replication	Experiments were replicated as indicated in the figure legends. All replication attempts were successful.
Randomization	Randomization was not applied to this study because it did not involve research subjects or participants. The study used in vitro assays that typically do not require randomization, where randomization (e.g. well positions) have no effect on the results. However, we ensured reproducibility and validity of the results by enforcing experimental rigor and the use of solid controls and standardized protocols.
Blinding	Biological analysis did not require any subjective analysis and thus did not require blinding.

Reporting for specific materials, systems and methods

We require information from authors about some types of materials, experimental systems and methods used in many studies. Here, indicate whether each material, system or method listed is relevant to your study. If you are not sure if a list item applies to your research, read the appropriate section before selecting a response.

Materials & experimental systems

n/a	Involved in the study	
☐	☒	Antibodies
☐	☒	Eukaryotic cell lines
☒	☐	Palaeontology and archaeology
☒	☐	Animals and other organisms
☒	☐	Clinical data
☒	☐	Dual use research of concern
☒	☐	Plants

Methods

n/a	Involved in the study	
☒	☐	ChIP-seq
☐	☒	Flow cytometry
☒	☐	MRI-based neuroimaging

Antibodies

Antibodies used	Mouse anti-His-Tag (clone HIS.H8, Invitrogen, MA121315, dilution 1:1000): https://www.thermofisher.com/antibody/product/6x-His-Tag-Antibody-clone-HIS-H8-Monoclonal/MA1-21315 Mouse anti-Flag (clone M2, Sigma-Aldrich, F1804; dilution 1:1000): https://www.sigmaaldrich.com/ES/es/product/sigma/f1804 Mouse anti-VSV-M (clone 23H12, Kerafast EB0011, dilution 1:1000): https://www.kerafast.com/productgroup/1011/anti-vsv-m-23h12-antibody?ProductID=445 Rabbit anti-DPEP1 antibody (Atlas Antibodies, HPA012783; dilution 1:100): https://www.atlasantibodies.com/products/primary-antibodies/triple-a-polyclonals/anti-dpep1-antibody-hpa012783/ Rabbit anti-GAPDH (Sigma-Aldrich, ABS16: dilution 1:3000): https://www.sigmaaldrich.com/ES/es/product/mm/abs16?srsltid=AfmBOoqCCqDdDyKEXCI3QVuzIrWmhZBsQ_h4A4aM6KYdoGtG4d_EZk40 HRP-conjugated anti-mouse (Invitrogen, G-21040, dilution 1:50000):https://www.thermofisher.com/antibody/product/Goat-anti-Mouse-IgG-H-L-Cross-Adsorbed-Secondary-Antibody-Polyclonal/G-21040 HRP-conjugated anti-rabbit (Invitrogen, G-21234, dilution 1:50000): https://www.thermofisher.com/antibody/product/Goat-anti-Rabbit-IgG-H-L-Cross-Adsorbed-Secondary-Antibody-Polyclonal/G-21234 IgG-AF647-conjugated anti-rabbit IgG antibody (Invitrogen, A32733, dilution 1:400): https://www.thermofisher.com/antibody/product/Goat-anti-Rabbit-IgG-H-L-Highly-Cross-Adsorbed-Secondary-Antibody-Polyclonal/A32733TR
Validation	All antibodies used in this study are comercially available and have been validated by the manufacturer (see websites indicated above for each antibody used), and used by other publications. Moreover, the specificity of the anti-Flag antibody was validated using cells transfected with an empty plasmid. The specificity of the anti-His antibody was validated using cells transfected with an empty plasmid or empty pseudotypes (see Extended Data Figure 5). The specificity of the DPEP1 antibody was validated by detecting signal specifically in DPEP1-incubated cells (Extended Data Figure 5).

Eukaryotic cell lines

Policy information about cell lines and Sex and Gender in Research

Cell line source(s)	The NCI-60 cell line panel was obtained from the National Cancer Institute. HEK293T cells were obtained from the Servicio Central de Soporte a la Investigación Experimental (SCSIE) from the University of Valencia. Expi293F cells were obtained from Thermo-Fischer (A14527). Schneider's Drosophila Line 2 (S2) cells were obtained from ATTC (CRL-1963). PK-15 cells were obtained from Cytion (607426). HEK293T-GFP1-10 and HEK293T-GFP11 cells were kindly provided by Olivier Schwartz (Institut Pasteur, Paris, France). Swine primary kidney cells (SPKC) were obtained from the National Veterinary Services Laboratories (NVSL). The sex of the pig SPKC donor is unknown.
Authentication	The 48 cell lines of the NCI-60 panel used in this study were authentificated by Short Tandem Repeat (STR) genotyping. The other cell lines were not authentificated.
Mycoplasma contamination	Cell lines were regularly shown to be free of mycoplasma contamination by PCR. Cells used for recombinant protein expression (Expi293F and S2) were not tested.
Commonly misidentified lines (See ICLAC register)	None.

Plants

Seed stocks	NA
Novel plant genotypes	NA
Authentication	NA

Flow Cytometry

Plots

Confirm that:

☒ The axis labels state the marker and fluorochrome used (e.g. CD4-FITC).

☒ The axis scales are clearly visible. Include numbers along axes only for bottom left plot of group (a 'group' is an analysis of identical markers).

☐ All plots are contour plots with outliers or pseudocolor plots.

☐ A numerical value for number of cells or percentage (with statistics) is provided.

Methodology

Sample preparation	Cells were detached gently with cold staining buffer (PBS, 0.5% BSA, 2mM EDTA) and incubated with serial dilutions of soluble recombinant human DPEP1 (Sino Biologicals) for 30 min at 4ºC. Cells were washed with PBS and incubated with an anti-DPEP1 antibody (Atlas Antibodies, HPA012783, dilution 1:100) for 30 min at 4ºC. After another wash with PBS, cells were incubated with a goat anti-rabbit IgG-AF647 secondary antibody (Invitrogen, A32733, dilution 1:400) for 30 min at 4ºC. Cells were fixed with 4% paraformaldehyde (PFA) for 10 min at room temperature, washed with PBS and resuspended in staining buffer.
Instrument	FACSVerse
Software	Collection: FACSSuite Analysis: FlowJo v10.10
Cell population abundance	At least 10.000 cells were acquired for each condition.
Gating strategy	Cells were only gated on live cells (FSC/SSC) and singlets (FSC-H/FSC-A). As this is a very simple and standard strategy, we did not include a supplementary figure showing it.

☒ Tick this box to confirm that a figure exemplifying the gating strategy is provided in the Supplementary Information.